nature communications

Article

https://doi.org/10.1038/s41467-025-63778-4

BMAL1-TRIM28 represses transposable elements independently of CLOCK in pluripotent cells

Received: 3 May 2024

Accepted: 27 August 2025

Published online: 10 September 2025

Check for updates

Amador Gallardo[1,2,3], Efres Belmonte-Reche[1,2,3,12], María Marti-Marimon[4,5,12], Joan Domingo-Reinés[1,2,3], Guillermo Peris[1,6], Lourdes López-Onieva[1,3,7], Iván Fernández-Rengel[1,2,3], Jiajun Xie[1,2,3], Pablo Tristán-Ramos[1], Nicolas Bellora[8], Antonio Sánchez-Pozo[1,2], Antonio M. Estévez[9], Sara R. Heras[1,2], Marc A. Marti-Renom[4,5,10,11] & David Landeira[1,2,3]

Circadian oscillations of gene transcripts rely on a negative feedback loop executed by the activating BMAL1-CLOCK heterodimer and its negative regulators PER and CRY. Although circadian rhythms and CLOCK protein are mostly absent during embryogenesis, the lack of BMAL1 during prenatal development causes an early aging phenotype during adulthood, suggesting that BMAL1 performs an unknown non-circadian function during organism development that is fundamental for healthy adult life. Here, we show that BMAL1 interacts with TRIM28 and facilitates H3K9me3-mediated repression of transposable elements in naïve pluripotent cells, and that the loss of BMAL1 function induces a widespread transcriptional activation of MERVL elements, 3D genome reorganization and the acquisition of totipotency-associated molecular and cellular features. We propose that during embryogenesis, BMAL1 is redeployed as a transcriptional repressor of transposons in a CLOCK-independent way, and the activity of BMAL1-TRIM28 during prenatal life might protect mammalian organisms from premature aging during adulthood.

Organisms that live on the surface of the earth are regulated by circadian rhythms that optimize their physiology during daily changes in sunlight[1]. In mammals, this is achieved through specialized photoreceptor cells in the retina that transmit information about light intensity to the brain, which then synchronizes peripheral molecular clocks present is most cells of the adult organism through humoral signals[1,2]. The molecular clock is based on a core heterodimeric complex composed by BMAL1 (Basic Helix-Loop-Helix ARNT Like 1) and CLOCK (clock circadian regulator) that activates transcription of its own negative regulators period circadian clock (Per1/2) and cryptochrome circadian regulator (Cry1/2) genes, generating a negative feedback loop that produces daily oscillations in the expression of up to 20 % of cellular transcripts in a tissue-specific way (also known as clock-controlled genes, CCGs)[3,4]. Dysregulation of CCGs during

[1]Centre for Genomics and Oncological Research (GENYO), Avenue de la Ilustración 114, 18016 Granada, Spain. [2]Department of Biochemistry and Molecular Biology II, Faculty of Pharmacy, University of Granada, Granada, Spain. [3]Instituto de Investigación Biosanitaria ibs.GRANADA, Granada, Spain. [4]Centre Nacional d'Anàlisi Genòmica, CNAG, Barcelona, Spain. [5]Centre for Genomic Regulation (CRG), Barcelona Institute of Science and Technology (BIST), Barcelona, Spain. [6]Department of Computer Languages and Systems, Universitat Jaume I, Castellón de la Plana 12071, Spain. [7]Department of Biochemistry and Molecular Biology I, Faculty of Sciences, University of Granada, Granada, Spain. [8]Laboratorio de Genómica Computacional, Instituto de Tecnologías Nucleares para la Salud (INTECNUS), Consejo Nacional de Investigaciones Científicas y Técnicas (CONICET), San Carlos de Bariloche, Argentina. [9]Instituto de Parasitología y Biomedicina "López-Neyra" (IPBLN), CSIC, Parque Tecnológico de Ciencias de la Salud, Avenida del Conocimiento, Armilla Granada, Spain. [10]Universitat Pompeu Fabra (UPF), Barcelona, Spain. [11]ICREA, Barcelona, Spain. [12]These authors contributed equally: Efres Belmonte-Reche, María Marti-Marimon. e-mail: davidlandeira@ugr.es

adulthood is commonly assumed to underlie the wide range of health disorders associated to malfunctioning of the circadian machinery[5–7]. However, the phenotypes of mice mutant for *Clock* and *Bmal1* genes are ostensibly dissimilar - altered metabolism and obesity in *Clock* mutant mice[8] versus early aging phenotype in *Bmal1*$^{-/-}$ specimens[9]. These different phenotypes indicate that many pathological conditions associated to the molecular clock might be a consequence of mutually independent functions of BMAL1 and CLOCK. Moreover, differences in the phenotypes of *Clock* and *Bmal1* mutant mice seem to emerge from the activity of BMAL1 during embryo development, because most of the phenotype observed in *Bmal1*$^{-/-}$ adult mice[9] is caused by the absence of BMAL1 during prenatal development, but not during adulthood[10]. Importantly, the molecular mechanism by which BMAL1 influences mouse development is unknown, but it is likely independent of its canonical function as an oscillator of gene transcription, because robust circadian oscillations of gene transcripts are not detected until perinatal stages when CLOCK protein becomes robustly expressed[11–18].

To investigate the alternative non-circadian function of BMAL1 during embryogenesis we focused our analysis on early stages of mouse development. Following fertilization, the mouse zygote divides, and its genome is activated, producing two totipotent cells (2C) that differentiate into embryonic or extraembryonic tissues[19]. The totipotent state is characterized by the expression of 2C-specific genes and Murine Endogenous Retroviral Element with a Leucine tRNA primer binding site retrotransposons (MuERV-L; also known as MERVLs), that are transcriptionally repressed when cells differentiate into either trophectoderm or the pluripotent inner cell mas (ICM) that form the early blastocyst[20,21]. The molecular basis of totipotency is poorly understood, due to difficulties in the isolation of totipotent cells directly from the 2C stage blastomeres[21]. However, cultures of pluripotent embryonic stem cells (mESCs) can be easily derived from the ICM of the blastocyst[22], and they contain a fraction of cells in a metastable state that display molecular features that resemble the totipotent 2 C blastomeres (2C-like cells (2CLC))[21,23]. Thus, mESCs cultures are an amenable in-vitro system to dissect the molecular basis of totipotency to pluripotency transition.

Here, we have examined the function of BMAL1 in naïve pluripotent mESCs. We show that BMAL1 interacts with TRIM28, facilitates H3K9me3 deposition and represses the transcription of transposable elements (TEs) in mESCs. Importantly, deletion of *Bmal1* leads to the transcriptional activation of MERVL copies, changes in the three-dimensional (3D) organization of the genome and acquisition of 2C-associated molecular and cellular features. Overall, we found that in the absence of high levels of CLOCK protein, BMAL1 is redeployed as a transcriptional repressor that regulates the expression of TEs and 3D genome organization in pluripotent cells. We propose that the activity of BMAL1 in partnership with TRIM28 during prenatal life might protect mammals from aging-associated diseases during adulthood.

Results

BMAL1 is required for the optimal recruitment of TRIM28 to chromatin

Analysis of our published mRNA sequencing (mRNA-seq) datasets of parental (JM8$^{+/+}$) and *Bmal1*$^{-/-}$ mESCs grown in the presence of Leukaemia-Inhibitory Factor and inhibitors of Mitogen-Activated Protein Kinase and Glycogen Synthase Kinase 3 (typically known as 2i+LIF media)[16] revealed that mis-expressed genes in *Bmal1*$^{-/-}$ cells are mostly over-expressed (454 upregulated vs 116 downregulated, FC > 2, $p < 0.05$) (Fig. 1A, Supplementary Data 1), suggesting that BMAL1 might be acting as a transcriptional repressor in the absence of CLOCK during early development. To address the molecular mechanism by which BMAL1 represses gene transcription in naïve mESCs we established a clonal cell line that expresses a FLAG-tagged version of BMAL1 (FLAG-BMAL1), isolated nuclei, and analysed the interactome of BMAL1 by anti-FLAG co-immunoprecipitation followed by mass spectrometry (Fig. S1A–S1C). We found that FLAG-BMAL1 interacts with factors involved in transcriptional repression (Supplementary Data 2) such as TRIM28 (also known as KAP1)[24], NACC1[25] and RIF1[26], and several zinc finger proteins (ZFPs) including ZFP638, ZFP326 and ZFP281 (Fig. S1D). We also identified interactions with proteins involved in rRNA production and mRNA splicing (Supplementary Data 2), but these were not further pursued because they are common contaminants in this type of purification schemes and neither rRNA expression nor mRNA splicing was affected in *Bmal1*$^{-/-}$ cells (Fig. S1E–S1G).

Among transcriptional repressors identified (Figure S1D), we focused on TRIM28 because it has a well-established role acting as a scaffold protein that recruits the chromatin regulators NuRD and SETDB1 to genomic regions[24,27–30]. As expected, protein coimmunoprecipitation followed by western blot confirmed that FLAG-BMAL1 and endogenous BMAL1 interact with TRIM28 (Fig. 1B–D). To address whether BMAL1 and TRIM28 bind to the same regions of the genome, and whether they are functionally linked, we performed calibrated (using a spike-in) chromatin immunoprecipitation followed by sequencing (cChIP-seq) using antibodies against BMAL1 or TRIM28 in JM8$^{+/+}$ parental wild-type and *Bmal1*$^{-/-}$ mESCs. Inspection of cChIP-seq signals in the genome browser revealed that BMAL1 and TRIM28 display a visually concordant distribution across the genome, although the accumulation of BMAL1 at punctate high-level target regions (usually referred to as binding peaks) is not so evident, as compared to the signal observed for TRIM28 (Fig. 1E). Importantly, we found that low-level ubiquitous signal of BMAL1 and TRIM28 binding to the genome in JM8$^{+/+}$ was lost in *Bmal1*$^{-/-}$ cells, demonstrating that BMAL1-TRIM28 complexes are present at DNA genomic regions that do not display binding peaks of these proteins (Fig. 1E). Genome-wide analyses showed a positive correlation between BMAL1 and TRIM28 binding (Fig. 1F and 1G), supporting that BMAL1 and TRIM28 have a largely overlapping distribution genome-wide. As expected, there was also a positive correlation in the binding signals of FLAG-BMAL1, BMAL1 and TRIM28 around the genome (Fig. S1H and S1I). Importantly, the genome-wide binding signal of TRIM28 was reduced in *Bmal1*$^{-/-}$ mESCs (Figs. 1H, I, S1J and S1K), indicating that BMAL1 is required for optimal recruitment of TRIM28 to chromatin. Of note, genes upregulated in *Bmal1*$^{-/-}$ mESCs (Fig. 1A) do not display TRIM28 binding peaks around their transcriptional start site (TSS) (Fig. 1J), suggesting that BMAL1-TRIM28 complexes repress the transcription of protein coding genes through a mechanism that does not require their accumulation at gene promoters.

BMAL1-TRIM28 modulates H3K9me3 levels and represses MERVL elements in mESCs

TRIM28 represses transcription of TEs in mESCs[31,32], and TEs can impact the regulation of protein-coding genes through several mechanisms[33]. Thus, we hypothesized that BMAL1-TRIM28 regulates the expression of TEs and indirectly modulate gene expression in mESCs. Peak calling analyses showed that regions with TRIM28 binding peaks mainly fell into repeated DNA sequences (1378 out of 1599), with a strong bias (1333 out of 1378) towards retrotransposons that contain long terminal repeats (LTRs) (Fig. 2A). Importantly, depletion of BMAL1 reduces the accumulation of TRIM28 at DNA repeats (Fig. 2B) and promotes a drastic transcriptional upregulation of TEs copies (1730 copies, FC > 2, $p < 0.05$) (Fig. 2C) (Supplementary Data 1), of which most (1399 out of 1730) were LTR retrotransposons (Fig. 2D). MERVL elements were particularly overrepresented among the over-expressed TEs (605 copies) (Fig. 2E). In agreement, we could readily detect transcriptional induction of 23,6% of all annotated MERVL copies (605 of 2555) in *Bmal1*$^{-/-}$ cells, suggesting the presence of BMAL1 is important to maintain full repression of MERVL elements across the genome. Induced copies represented 79.6%

https://doi.org/10.1038/s41467-025-63778-4

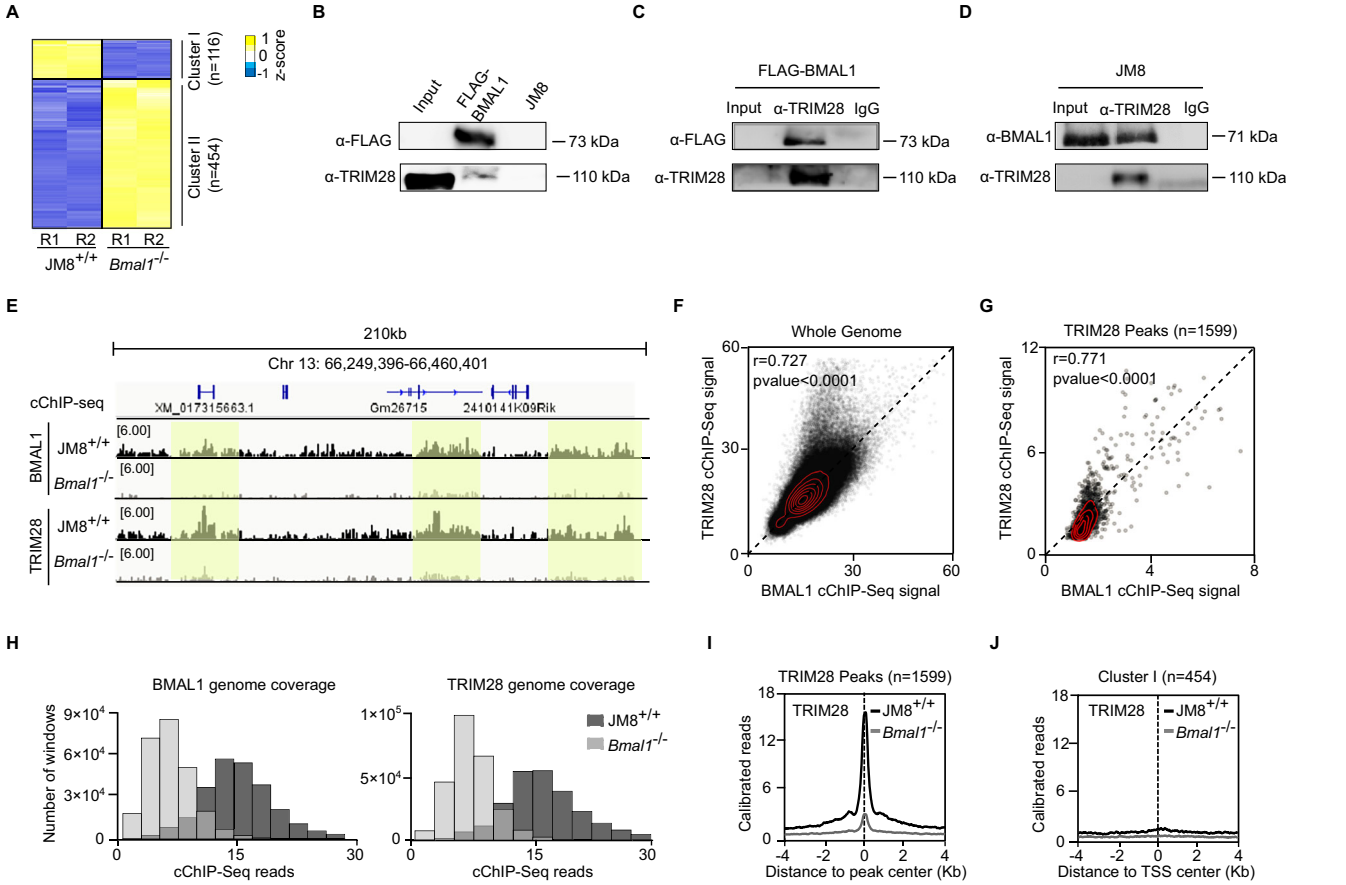

Fig. 1 | BMAL1 is required for TRIM28 binding to chromatin. A Heatmap of genes mis-expressed in *Bmal1*$^{-/-}$ compared to wild-type JM8$^{+/+}$ mESCs analysed by mRNA-seq (FC > 2 and $p < 0.05$; Wald test with Benjamini-Hochberg correction). Yellow and blue colours indicate Z-scores (deviation from the mean). R1 and R2 denote biological replicates. **B** Co-immunoprecipitation showing the interaction between BMAL1 and TRIM28 in FLAG-BMAL1-expressing mESCs. Anti-FLAG antibody was used to pull down FLAG-BMAL1 from nuclear extracts, and TRIM28 was detected by western-blot. Anti-FLAG IP in JM8$^{+/+}$ mESCs served as a negative control. Input: 10% of lysate. **C** As in **B**, but TRIM28 was immunoprecipitated with an anti-TRIM28 antibody and the interaction with FLAG-BMAL1 was detected with an anti-FLAG antibody. IgG immunoprecipitation served as a negative control. Input: 1% of the lysate. **D** Co-immunoprecipitation analysis of TRIM28 and endogenous BMAL1 in nuclear extracts of JM8 mESCs. TRIM28 was immunoprecipitated with an anti-TRIM28 antibody and the interaction with endogenous BMAL1 was detected with an anti-BMAL1 antibody. IgG immunoprecipitation served as a negative control. Input: 1% of the lysate. **E** Genome browser view of BMAL1 and TRIM28 binding profiles in JM8$^{+/+}$ and *Bmal1*$^{-/-}$ mESCs. Light yellow boxes highlight regions with punctate enrichment of BMAL1 and TRIM28. **F** Correlation of BMAL1 and TRIM28 cChIP−seq signals genome-wide. The genome was divided into 10-kb windows; total reads per window were plotted. Pearson's r and p-values are indicated. **G** Correlation of BMAL1 and TRIM28 cChIP−seq signals at TRIM28 peaks ($n = 1599$). Pearson's r and *p*-values are indicated. (**H**) Histogram of BMAL1 and TRIM28 signal distribution in JM8$^{+/+}$ and *Bmal1*$^{-/-}$ mESCs. The number of windows with a given total read count (10-kb bins) is shown. **I** Average binding profiles of TRIM28 in JM8$^{+/+}$ and *Bmal1*$^{-/-}$ mESCs centred on TRIM28 binding peaks ($n = 1599$) identified in JM8$^{+/+}$ cells. **J** Average binding profiles of TRIM28 in JM8$^{+/+}$ and *Bmal1*$^{-/-}$ mESCs around the TSS of genes that are upregulated in Bmal1$^{-/-}$ mESCs ($n = 454$). At least two biologically independent experiments were performed in B-D. Source data are provided in the Source Data file.

of all MERVL elements measurable in our experiment (605 out of 760 copies). Notably, out of the 594 full-length copies annotated in the reference genome, we could analyse the expression of 453 copies, of which 406 (89.62%) were transcriptionally induced (FC > 2, $p < 0.05$) (Fig. S2A). Finally, family-based analysis by mRNA-seq (Fig. S2B and S2C) and RT-qPCR (Figure S2D) confirmed that BMAL1 is required to repress MERVL elements. Taken together, these analyses support that BMAL1 is involved in the transcriptional repression of full-length MERVL elements genome-wide in naïve mESC.

TRIM28 interacts with SETDB1 and facilitates methylation of H3K9 and transcriptional repression of endogenous retroviruses (ERVs) in mESCs[28,31,32]. Thus, we hypothesized that in the absence BMAL1 and efficient TRIM28 binding (Fig. 1H and 1I), the distribution of H3K9me3 would be perturbed and facilitate transcriptional upregulation of MERVL elements. Global levels of TRIM28 protein and H3K9me3 remain mostly unaltered in BMAL1-depleted cells (Fig. S2E). However, their pattern of accumulation within the nucleus (Figure S2F and S2G) and their presence on chromatin genome-wide (Fig. 1H and S2H) was altered in *Bmal1* $^{-/-}$ cells compared to JM8$^{+/+}$ cells. In consonance, in the absence of BMAL1, binding of TRIM28 was reduced at many families of TEs (Fig. 2F). However, reduced TRIM28 binding was associated to decreased H3K9me3 and increased mRNA synthesis distinctively at MERVL elements (Fig. 2F), indicating that BMAL1 is critical for maintaining transcriptional repression mostly at MERVL elements in mESCs. In keeping, enrichment analyses of TRIM28 binding and H3K9me3 decoration along MERVL and solo LTR sequences (consensus and full-length MERVL elements) using multi-hit reads confirmed their reduction in *Bmal1*$^{-/-}$ cells compared to JM8$^{+/+}$ cells (Fig. 2G and 2H). Of note, enrichment of TRIM28 at MERVL elements was low compared to TRIM28 binding peaks and other targets of TRIM28 such as intracisternal A-type particles (IAP) transposons[32] (compare scales in Figs. 2H and Fig. 1I), indicating that transcriptional repression of MERVL depends on BMAL1-TRIM28 activity that does not require formation of

https://doi.org/10.1038/s41467-025-63778-4

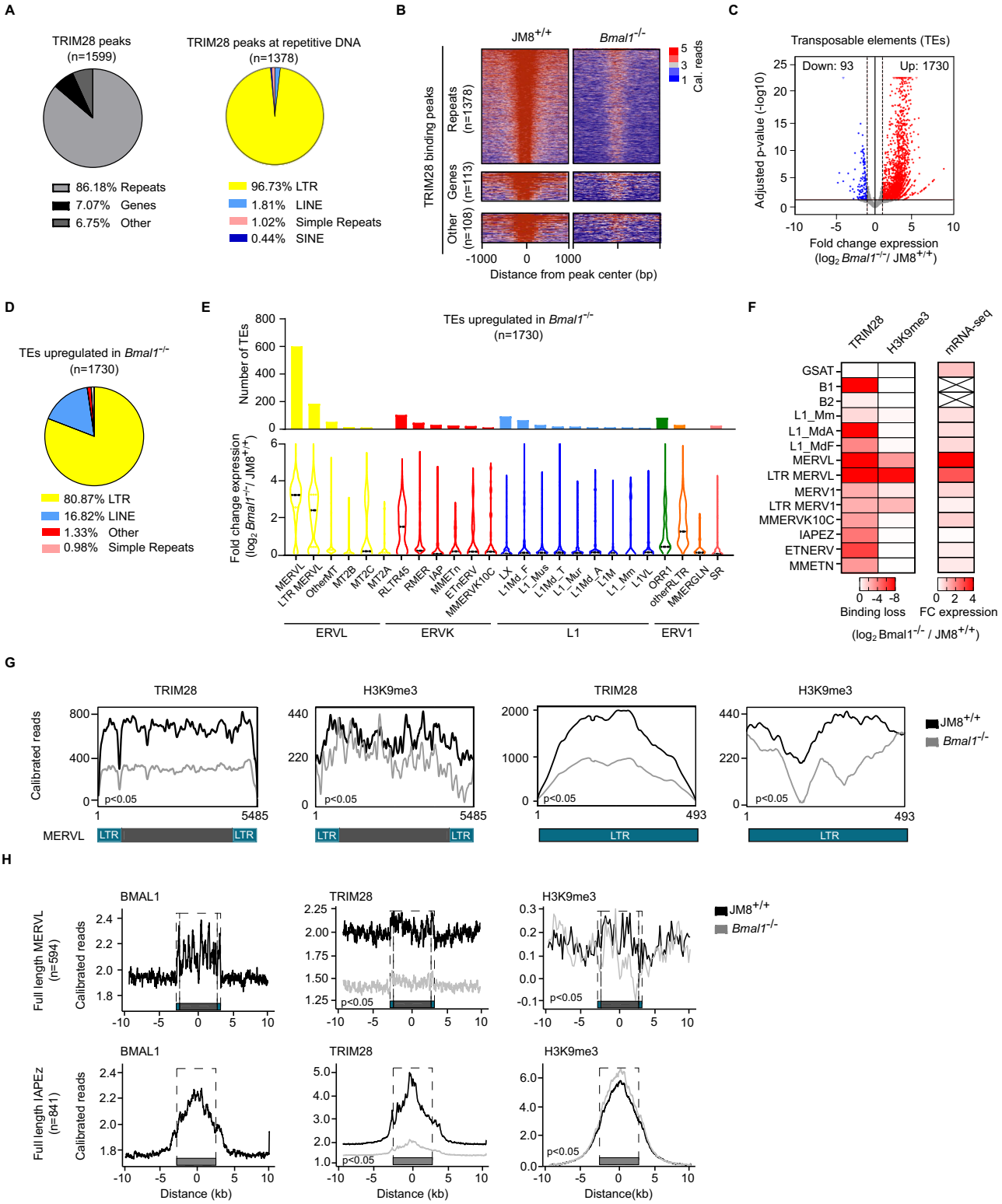

large genomic domains enriched for TRIM28 and H3K9me3 (Fig. S2I). Expression of H3K9 methyltransferases and demethylases was unaltered in *Bmal1*$^{-/-}$ cells (Fig. S2J), discarding that deregulation of MERVLs in *Bmal1*$^{-/-}$ cells is an indirect effect of transcriptional mis-expression of genes involved in H3K9 methylation. Thus, we concluded that BMAL1 is required for efficient binding of TRIM28 to chromatin, maintenance of H3K9me3 levels and preservation of the transcriptionally repressed state of MERVL retrotransposons in mESCs.

Transcriptional activation of MERVLs and neighbouring genes is associated to changes in 3D chromatin organization in *Bmal1*$^{-/-}$ mESCs

Genes upregulated in *Bmal1*$^{-/-}$ cells (Fig. 1A) tend to be in linear proximity of upregulated MERVLs (median distance 121 Kb) as compared to unaltered control genes (median distance 637 Kb) (Fig. 3A and 3B), supporting that production of RNA coming from MERVL and nearby genes is co-regulated *in cis*. Based on previous literature, we

Fig. 2 | BMAL1 facilitates binding of TRIM28, H3K9me3 labelling, and transcriptional repression of MERVL elements in mESCs. A Genomic distribution of TRIM28 binding peaks. **B** Heatmap comparing TRIM28 binding signal (calibrated reads) in JM8$^{+/+}$ and *Bmal1*$^{-/-}$ mESCs around the centre of regions bound by TRIM28 in JM8$^{+/+}$ cells and classified in indicated categories. **C** Volcano plot showing the expression level of individual TEs in *Bmal1*$^{-/-}$ relative to JM8$^{+/+}$ mESCs. Significantly upregulated (FC > 2, $p < 0.05$, red colour), downregulated (FC < 2, $p < 0.05$, blue colour) or unchanged (grey colour) TEs are shown. p-values were calculated by Wald test with Benjamini-Hochberg correction. (**D**) Pie chart showing the classification of the 1730 TEs that are overexpressed in *Bmal1*$^{-/-}$ mESCs. **E** Top panel shows a bar plot displaying the subfamily classification of the 1730 TEs that are overexpressed in *Bmal1*$^{-/-}$ mESCs. Bottom panel is a violin plot showing the median upregulation (log_2 fold change expression of Bmal1$^{-/-}$ versus Jm8$^{+/+}$) of individual TEs grouped by subfamily. **F** Heatmap showing the reduction of TRIM28 and H3K9me3 enrichment (as assayed by cChIP-seq) and the increase in mRNA expression (measured by mRNA-seq) in *Bmal1*$^{-/-}$ relative to JM8$^{+/+}$ at the consensus sequence of indicated families of TEs. **G** Plots displaying the TRIM28 and H3K9me3 enrichment signals along the consensus sequence of full MERVL (left panels) or MERVL-specific LTR (also known as MT2_mm) elements (right panels) in JM8$^{+/+}$ and *Bmal1*$^{-/-}$ mESCs. *p*-values calculated by two-way ANOVA. **H** Plots displaying the average BMAL1, TRIM28 and H3K9me3 enrichment profile along the genomic regions containing the full length MERVL (as previously defined[86], $n = 594$) (top panel) or IAPEz copies (longer than 5Kb, $n = 841$) (bottom panel). *p*-values calculated by a two-way ANOVA. Source data are provided as a Source Data file.

hypothesized that co-regulation of genes and MERVL elements could be based on the production of MERVL-containing chimeric transcripts[23,34] or be associated to changes in 3D chromatin organization[35,36].

To test the former hypothesis, we identified TEs-chimeric RNAs produced in *Bmal1*$^{-/-}$ mESCs and determined that MERVL containing chimeric RNAs expressed in *Bmal1*$^{-/-}$ did not match the sequences of protein coding genes upregulated in *Bmal1*$^{-/-}$ cells (Fig. 3C). In addition, distance- and strand-specific analysis of the closest protein coding gene TSS located upstream or downstream of upregulated MERVLs (605 MERVL copies with FC > 2, $p < 0.05$) supported that the 454 genes upregulated in *Bmal1*$^{-/-}$ mESCs are not the result of chimeric transcription, because they are not located in linearly adjacent positions to upregulated MERVLs (Fig. S3A–C). In agreement, MERVLs and solo LTRs that are transcriptionally-induced in *Bmal1*$^{-/-}$ mESCs could be classified mostly as self-dependent, because they are encoded in intergenic regions or within gene bodies of protein coding genes that were not transcriptionally activated in *Bmal1*$^{-/-}$ mESCs (Fig. S3D). Taken together, we concluded that the *in cis* co-regulation of MERVLs and protein-coding genes in *Bmal1*$^{-/-}$ cells is not mediated by the synthesis of MERVL-containing chimeric transcripts.

To study whether 3D genome organization underlies the co-regulation of MERVLs and protein coding genes observed in *Bmal1*$^{-/-}$ cells we first annotated mis-expressed elements using a karyotype-like representation of their genomic position. Over-expressed genes and MERVL copies in *Bmal1*$^{-/-}$ cells were located throughout all chromosomes but tend to cluster at some genomic positions where genes and MERVLs were coordinately activated (Fig. S3E). For example, transcriptional induction of the six *Zscan4* genes occurred concurrently with the activation of three interspersed MERVL copies (Fig. S3F). To analyse whether changes in 3D genome organization relate to the concordant transcriptional induction of nearly located MERVLs and genes, we compared chromatin organization using chromosome conformation capture[37] followed by sequencing (Hi-C)[38] in *Bmal1*$^{-/-}$ and parental JM8$^{+/+}$ cells. *Bmal1*$^{-/-}$ cells display decreased intra-chromosomal interactions and concomitant increase in inter-chromosomal contacts, suggesting that BMAL1 may be necessary to maintain an overall chromosome-wide chromatin structure in mESCs (Fig. 3D and S4A). We then asked whether BMAL1 is involved in the compartmentalization of chromosomes in the so-called "A" and "B" compartments (enriched in "active" or "repressive" chromatin respectively). We found that depletion of BMAL1 promotes increased compartment strength (Fig. 3E) due to enhanced homotypic interactions between sequences belonging to the A compartment (Figs. 3F, 3G and S4B). Moreover, a subset of genomic regions (2.14%) transited from the "repressed" B to "active" A compartment upon deletion of *Bmal1* (Fig. 3G), suggesting that the transcriptional activation of TEs and/or genes induced by BMAL1 depletion was accompanied by the migration of their genomic sequences towards the A compartment. In agreement, 605 MERVL copies ($log_2FC > 1$, $p < 0.05$) and 273 protein coding genes ($log_2FC > 1.5$, $p < 0.05$) that were transcriptionally induced in *Bmal1*$^{-/-}$ mESCs showed a tendency to be relocated to the A compartment, as compared to non-induced controls (Fig. 3H). In contrast, analysis of the structure of topological associating domains (TADs) in *Bmal1*$^{-/-}$ and parental JM8$^{+/+}$ cells revealed no major differences (Fig. S4C and S4D). We concluded that depletion of BMAL1 in mESCs leads to the transcriptional activation of MERVL retrotransposons and neighbouring genes through a mechanism that involves their repositioning towards chromatin compartment A (Fig. 3I), where they may find the factors that facilitate more efficient RNA transcription.

Bmal1$^{-/-}$ mESCs display 2C-specific molecular and cellular features

MERVLs and ZSCAN4 are expressed in 2 C embryos, and they are downregulated in pluripotent cells[39,40]. Thus, augmented expression of these two totipotency markers in *Bmal1*$^{-/-}$ mESCs cultures (Fig. 2E and S3F) suggested that depletion of BMAL1 destabilizes pluripotent cell identity, and cells transit back to a 2CLC state (Fig. 4A). In support of this hypothesis, we found that deletion of *Bmal1* favours the activation of the 2 C transcriptional programme (Fig. 4B). This includes the upregulation of 2 C marker genes such as *Zscan4*, *Dux*, *Dub1*, *Tcstv1*, *Tcstv3 and Eif1a* (Figs. 4C and 2A), that is translated into a significant increase of ZSCAN4 protein in *Bmal1*$^{-/-}$ cells compared to JM8$^{+/+}$ (Fig.s. 4D–F) and acquisition of a single enlarged immature nucleolus (Fig. 4G and H), as previously described for 2 C cells[41]. Moreover, *Bmal1*$^{-/-}$ cells display enhanced propensity to activate extraembryonic trophectoderm markers (*Cdx2*, *Gata3*, *Mmp9* and *Elf5*) than wild-type mESCs upon plating in differentiation media (Fig. 4I and J). Similar results were obtained with independently derived *Bmal1*$^{-/-}$#2 mESCs (Fig. S5B–F). Taken together, we concluded that BMAL1-mediated repression of MERVLs and 2C-associated genes prevents the reversion of pluripotent mESCs towards a 2CLC-state.

BMAL1-mediated repression of 2CLC-specific features does not require CLOCK protein

We wondered whether BMAL1 requires interaction with CLOCK to repress MERVL elements and 2C-associated genes in mESCs. It has been proposed that CLOCK protein is not expressed in mESCs[18], and that the absence of a functional BMAL1-CLOCK heterodimer impedes the production of circadian oscillations in this cell type[14]. In consonance, we detected very low expression of CLOCK protein in wild type mESCs compared to mouse neural stem cells (NSCs) where the circadian clock is functional (Figs. 5A and S6A). We hypothesized that in the absence of the right stoichiometric amount of CLOCK protein, BMAL1 interacts with TRIM28 and carries out a CLOCK-independent alternative function. To challenge this model, we depleted CLOCK protein by generating *Clock*$^{-/-}$ mESCs using CRISPR/Cas9 (Figs. 5B and S6B), confirmed that they express pluripotency-associated features (Fig. S6C–G), and study whether depletion of CLOCK recapitulated the alterations observed in *Bmal1*$^{-/-}$ mESCs. In

https://doi.org/10.1038/s41467-025-63778-4

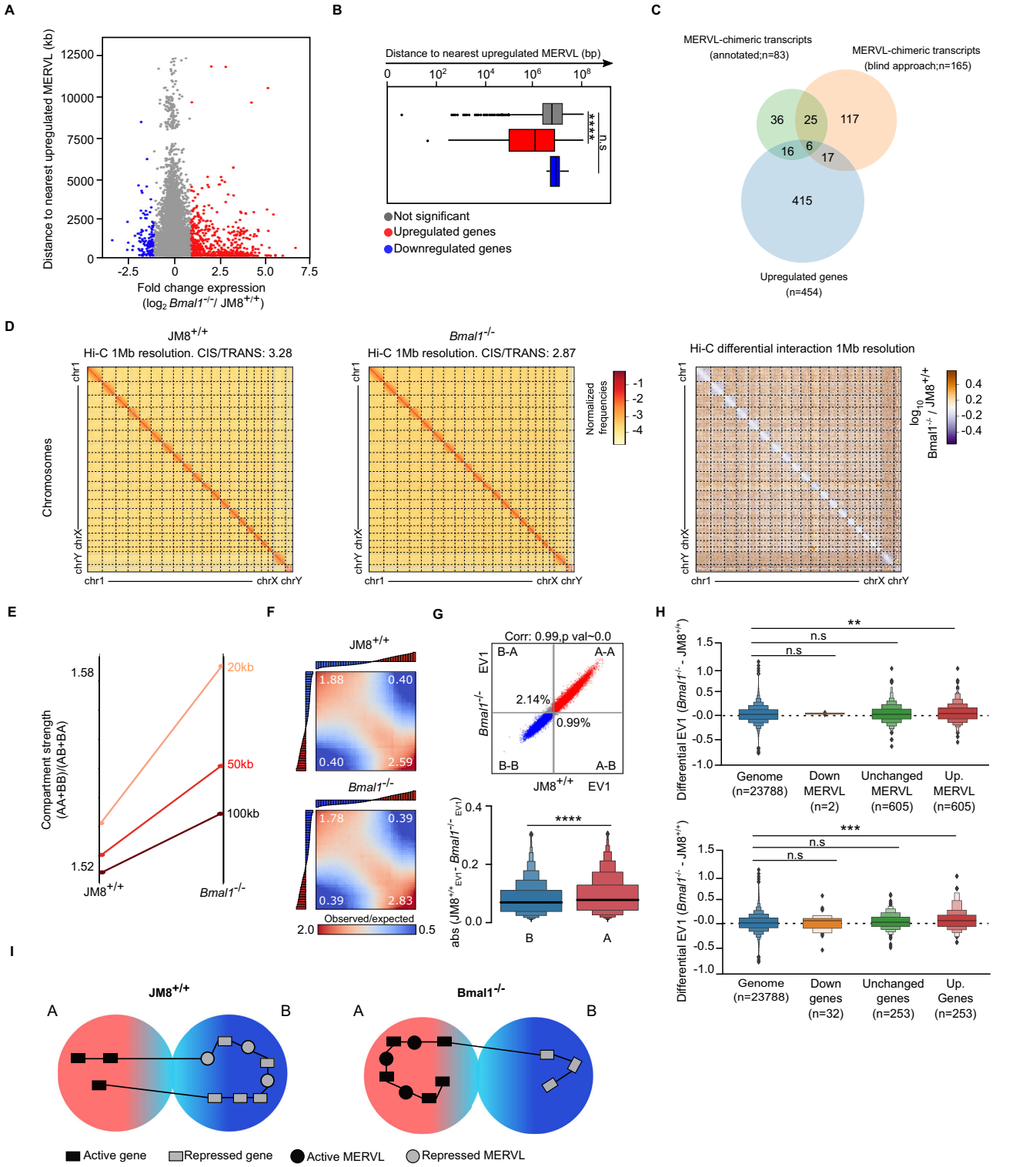

contrast to the phenotype observed in *Bmal1*$^{-/-}$ cells, the lack of CLOCK protein did not affect the nuclear distribution of TRIM28 protein nor the formation of H3K9me3-labelled heterochromatin *foci* (Fig. 5C). Importantly, mRNA-seq analysis demonstrated that neither MERVL elements, nor any other TE family, were upregulated in *Clock*$^{-/-}$ cells compared to the JM8$^{+/+}$ cell line (Figs 5D, S6H and S6I). The lack of CLOCK protein resulted in the over-expression of 248 protein coding genes (FC > 2, $p < 0.05$), which were mostly unaffected in *Bmal1*$^{-/-}$ cells (Fig. 5E). In addition, 2C-associated genes were not over-expressed in *Clock*$^{-/-}$ cells (Figs. 5F and G), the level of ZSCAN4 protein was unaltered (Fig. 5H), and the nucleolar organization did not acquire a 2C-typical large nucleolar distribution (Fig. 5I and J). We concluded that BMAL1 does not require CLOCK protein to repress MERVL TEs nor 2C-associated genes in mESCs. Overall, our results support a model in which interaction between BMAL1 and TRIM28 during prenatal development helps to establish cell-type-specific gene expression programmes, while interaction between BMAL1 and CLOCK after birth mediate circadian oscillations of gene transcripts.

Fig. 3 | Transcriptional activation of MERVL retrotransposons and neighbouring genes is associated with altered 3D chromatin organization in *Bmal1*$^{-/-}$ mESCs. A Plot showing the expression of protein-coding genes in *Bmal1*$^{-/-}$ cells versus JM8$^{+/+}$ (x-axis) relative to their distance to the nearest upregulated MERVL in *Bmal1*$^{-/-}$ mESCs. Genes upregulated (FC > 2, $p < 0.05$) or downregulated (FC < 2, $p < 0.05$) are shown in red and blue, respectively. *p*-values were calculated by Wald test with Benjamini-Hochberg correction. **B** Boxplot comparing the distance between mis-expressed genes and the nearest upregulated MERVL in *Bmal1*$^{-/-}$ cells. Genes are grouped as upregulated (FC > 2, $p < 0.05$), downregulated (FC < 2, $p < 0.05$), or unchanged. Statistical differences were assessed by two-tailed Kruskal–Wallis test. Boxes show IQR with median; whiskers extend to 1.5× IQR; outliers as points. **C** Venn diagram showing the overlap between expressed MERVL-containing chimeric RNA transcripts and transcriptionally upregulated genes in *Bmal1*$^{-/-}$ mESCs. **D** Genome-wide Hi-C interaction maps at 1 Mb resolution for JM8$^{+/+}$ and *Bmal1*$^{-/-}$ cells (left and middle panels). Right: differential interaction (ratio) map. **E** Plot comparing the compartment strength at the indicated resolutions. **F** Saddle plots showing **A** (red) and **B** (blue) compartment interactions (100 kb bins) ranked by eigenvector. **G** Correlation of eigenvector values between JM8$^{+/+}$ and *Bmal1*$^{-/-}$ cells for genomic bins (100 kb) remaining in A (red), B (blue) or switching compartments (grey) (top). The percentage of changing bins is indicated. Bottom: distribution of eigenvector difference (absolute value of JM8$^{+/+}$ minus *Bmal1*$^{-/-}$ signal) for bins classified as A (red) or B (blue) in *Bmal1*$^{-/-}$ cells. Median is depicted as a line. Statistical difference was assayed by two-tailed Mann-Whitney test. **H** Top: compartment changes (eigenvector differences) for bins (100 kb) covering all genomic regions, downregulated ($\log_2$FC < −1, $p < 0.05$), upregulated ($\log_2$FC > 1, $p < 0.05$) or unchanged MERVL elements in *Bmal1*$^{-/-}$ cells. Bottom: compartment changes for protein-coding genes that are downregulated ($\log_2$FC < −1.5, $p < 0.05$), upregulated ($\log_2$FC > 1.5, $p < 0.05$) or unchanged in *Bmal1*$^{-/-}$ cells. Median represented as line, outliers as dots. Two-tailed Kruskal–Wallis test was used. **I** Model proposing how loss of BMAL1 induces a coordinated redistribution of MERVL elements and protein-coding genes into A compartments, where their transcription is activated. In **B**, **G** and **H** significance is indicated: $^{**}p < 0.01$, $^{***}p < 0.001$ and $^{****}p < 0.0001$. Data in **D**-**H** are from two combined independent Hi-C experiments.

Discussion

It is now almost two decades ago that the opposing phenotypes of *Clock* and *Bmal1* mutant mice were reported; altered metabolism and obesity in *Clock* mutant mice[8] versus a drastic progeria-like syndrome in *Bmal1*$^{-/-}$ adults[9]. This discrepancy was further exacerbated by a more recent report by the Fitzgerald lab demonstrating that the early aging phenotype of *Bmal1*$^{-/-}$ mice is mostly due to the function of BMAL1 protein during prenatal development[10], when CLOCK is not expressed and circadian oscillations are absent[14,18]. Together, these discoveries raised the fundamental question as to what the function of BMAL1 during embryo development is. In this study, we demonstrate that BMAL1 interacts with TRIM28 and facilitates H3K9me3-mediated repression of MERVL TEs in naïve pluripotent cells, and that the loss of BMAL1 function induces a widespread transcriptional activation of MERVL elements, 3D genome reorganization and the acquisition of 2C-associated molecular and cellular features. Thus, our findings indicate that during early development, BMAL1 is redeployed as a transcriptional repressor of TEs and suggest that this CLOCK-independent function might be a key molecular pathway underlying the early aging phenotype observed in *Bmal1*$^{-/-}$ adult mice.

Our proteomic analysis indicates that BMAL1 interacts with the transcriptional regulators TRIM28 and RIF1 in naïve mESCs, and our functional analyses demonstrate that depletion of BMAL1 impairs TRIM28 binding and H3K9me3 accumulation at MERVL elements, resulting in augmented production of MERVL transcripts. These findings are in fitting with previous reports that support that both TRIM28 and RIF1 can repress transcription of ERVs through SETDB1 and H3K9 methylation[26,31,32,42]. In addition, the phenotype of *Bmal1*$^{-/-}$ mESCs is also similar to the one described in RIF1 and SETDB1 null mESCs at the cellular level[43–46], because the three mutant cell lines display overt activation of 2C-associated genes, and higher efficiency of differentiation towards extraembryonic lineages. The main difference between the phenotypes of *Bmal1*, *Trim28* and *SetdB1* knockout pluripotent cells is that while the loss of TRIM28 and SETDB1 is incompatible with pluripotency maintenance and early embryogenesis[32,47–49], the lack of BMAL1 does not fully impair pluripotent self-renewal nor embryo development[9,16,17]. The milder phenotype observed upon *Bmal1* deletion is probably a consequence of the recruitment of TRIM28 and SETDB1 to chromatin through BMAL1-independent mechanisms, such as the ones involving ZFPs that contain a Krüppel-associated box domain (KRAB-ZFPs)[24], or other factors that might specifically operate during early development[50,51]. In fitting, while deletion of *Trim28* leads to a wide overexpression of TEs of different families in mESCs[32], we found that the depletion of BMAL1 mostly influences a specific subset of them.

Although in this study we demonstrate that BMAL1 is required for optimal recruitment of TRIM28 on chromatin in naïve mESCs, the details of the molecular interplay between these two proteins are unclear. TRIM28 does not directly bind to DNA, but it is generally recruited to DNA by KRAB-ZFPs[24], which bind DNA through their zinc finger domains and recruit TRIM28 through interaction with their KRAB domain[24]. Because BMAL1 harbours no standalone DNA-binding nor annotated KRAB domains, deciphering the mechanistic details as to how BMAL1 facilitates binding of TRIM28 to chromatin is complex and will require further studies. In this context, it might be relevant to highlight that the BMAL1-CLOCK heterodimer is recruited to E-box-containing promoters through the DNA-binding domain that is formed by the two complementary basic helix-loop-helix (bHLH) motifs contained in each of the heterodimer partners[52]. Thus, it is possible that in the absence of CLOCK protein, the standalone bHLH motif of BMAL1 facilitates interactions with MERVL-encoding DNA. Alternatively, BMAL1-TRIM28 might be recruited to MERVL elements through the DNA-binding ZFPs that we detected as BMAL1 interactors in proteomic analyses (ZFP638, ZFP281 and ZFP326).

The expression of MERVLs is strictly regulated during mouse early development, and it is commonly used as a marker of totipotency that is distinctly lost in pluripotent cells[21]. However, the molecular mechanism by which MERVL elements favour the totipotent state is poorly understood, and it has been suggested that it involves the synthesis of MERVL-chimeric transcripts[23,34], direct modulation of OCT4 and SOX2 levels[53], and changes in the 3D organization of the genome[35,36]. In this context, we found that transcriptional activation of MERVL copies and 2C-associated genes in *Bmal1*$^{-/-}$ mESCs grown in 2i +LIF is not induced by altered levels of OCT4 protein nor production of MERVL-containing chimeric transcripts, but maybe through a *in cis* co-regulation mechanism that involves changes in 3D genome organization. This idea is sustained by our Hi-C analysis showing repositioning of transcriptionally induced MERVL elements and protein coding genes towards the A compartment. In addition, in contrast to previous reports analysing 2C embryos[54–56] or CAF-1-depleted 2CLCs[36], our analyses revealed no genome-wide decrease of insulation nor formation of new insulation borders due to MERVL activation. Thus, we propose that although full reprogramming of pluripotent chromatin towards totipotency might involve global changes in insulation, formation of MERVL-associated TADs and changes in chromatin compartments, the impact of BMAL1 deletion only induces specific changes in compartmentalization. Consequently, *Bmal1*$^{-/-}$ mESCs grown in 2i+LIF seem to reside in an intermediate state between pluripotency and totipotency, characterized by simultaneous expression of MERVL elements and 2C-specific genes together with a high level of the pluripotency-associated factor OCT4. Similar intermediate cell states between totipotency and pluripotency have also been reported upon forced expression of DUX protein[57] or deletion of the H3K9 methyltransferase SetDB1[46]. To confirm the role of BMAL1 during

https://doi.org/10.1038/s41467-025-63778-4

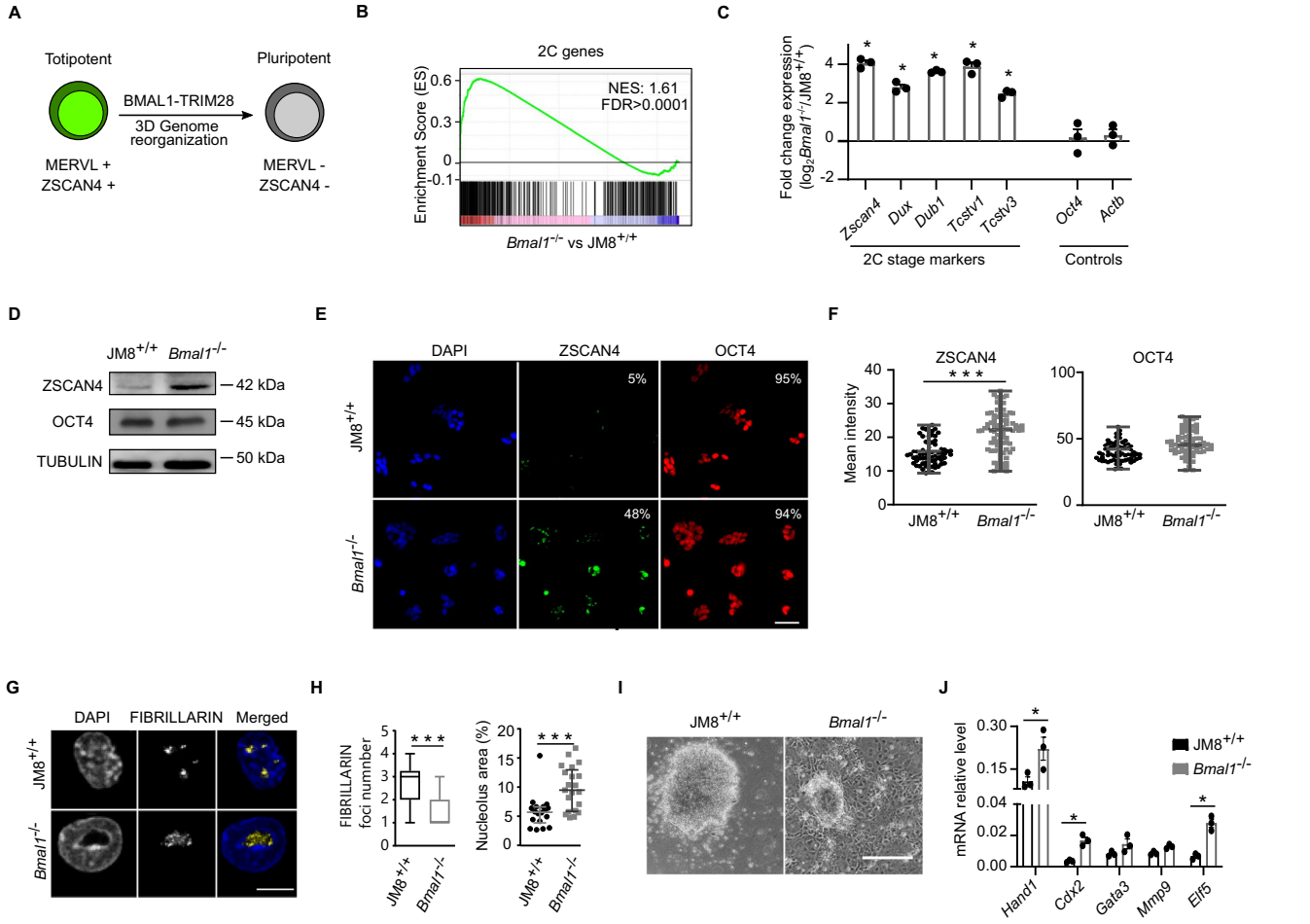

Fig. 4 | *Bmal1*$^{-/-}$ mESCs display 2C-specific molecular and cellular features. **A** Diagram proposing a mechanism by which BMAL1-TRIM28 facilitates the totipotent to pluripotent transition. **B** Gene Set Enrichment Analysis of the 2C-associated gene expression programme in *Bmal1*$^{-/-}$ mESCs. Normalized Enrichment Score (NES) and FDR are indicated. **C** Analysis of mRNA expression by RT-qPCR of 2C-associated genes in *Bmal1*-/- relative to JM8$^{+/+}$ mESCs. Gene expression was normalized to housekeeping genes (*Hmbs*, *Ywhaz*). *Oct4* and *Actb* were included as controls. Mean ± SEM of three experiments is shown. Asterisks indicate $p < 0.05$ in two-tailed Mann-Whitney test. **D** Western blot of whole cell lysates showing ZSCAN4 and OCT4 in JM8$^{+/+}$ and *Bmal1*$^{-/-}$ mESCs. TUBULIN was used as a loading control. Two biological replicates were performed. **E** Immunofluorescence images of DAPI (blue), ZSCAN4 (green) and OCT4 (red) staining in JM8$^{+/+}$ and *Bmal1*$^{-/-}$ mESCs. The percentage of cells positive for ZSCAN4 or OCT4 labelling is indicated ($n = 80$). Scale bar is 100 μm. **F** Plot showing the mean intensity of ZSCAN4 and OCT4 in JM8$^{+/+}$ and *Bmal1*$^{-/-}$ mESCs ($n = 80$ cells per genotype). Asterisks indicate $p < 0.0001$ in two-tailed Mann-Whitney test. Horizontal line indicates median, bars full data range. **G** Immunofluorescence images of the nucleolar protein FIBRILLARIN and DAPI staining in JM8$^{+/+}$ and *Bmal1*$^{-/-}$ mESCs. Scale bar is 10 μm. **H** Boxplots showing the number of FIBRILLARIN-positive foci per cell (left panel), and the percentage of the area of the nucleus that they occupy (right panel) in JM8$^{+/+}$ and *Bmal1*$^{-/-}$ mESCs ($n = 30$ cells per genotype). Medians are shown, left panel displays full range, right panel IQR. Asterisks indicate $p < 0.0001$ in two-tailed Mann-Whitney test. **I** Brightfield microscopy images of JM8$^{+/+}$ and *Bmal1*$^{-/-}$ mESCs after 14 days of growth at low density in ESCs media lacking ERK/GSK3 inhibitors but containing serum/LIF, allowing spontaneous differentiation towards trophectoderm. Scale bar is 100 μm. **J** Gene expression analysis by RT-qPCR of trophectoderm-associated genes in JM8$^{+/+}$ and *Bmal1*$^{-/-}$ mESCs described in (**I**). mRNA expression was normalized to *Hmbs* and *Ywhaz* housekeeping genes. Mean ± SEM of three experiments is shown. Asterisks indicate $p < 0.05$ in two-tailed Mann-Whitney test. Source data are provided as a Source Data file.

totipotency to pluripotency transition, it will be necessary to analyse the effect of the loss of function of BMAL1 in preimplantation embryos. This experiment will require a careful setup because sterile *Bmal1*$^{-/-}$ mice are generated by crossing *Bmal1*$^{+/-}$ mice[9], and it is probable that oocyte-synthesize *Bmal1* transcript and protein are present during initial embryo cleavages[11], rescuing the absence of zygote-derived *Bmal1* mRNA in *Bmal1*$^{-/-}$ mouse embryos during early development.

Independently of the molecular details explaining the regulatory relationship between MERVL and 2C-associated genes during early development, our results provide solid evidence that the transcriptional repression of MERVL elements by BMAL1-TRIM28 is functionally independent of CLOCK. This suggests that the low expression of CLOCK protein observed during mouse development[18] facilitates non-circadian alternative interactions between BMAL1 and H3K9me3-related proteins (TRIM28 and RIF1) during embryogenesis. However, we cannot rule out that BMAL1 represses TEs through interaction with TRIM28 in other contexts in which CLOCK protein is present and circadian expression is taking place, because a fraction of BMAL1 monomers might not form activating complexes with CLOCK and would interact with TRIM28 instead. In consonance, a recent study has shown that BMAL1 interacts with TRIM28 to repress the transcription of LINE1 TEs in human mesenchymal stem cells (hMSCs) derived from adult bone marrow[58].

To conclude, we propose that BMAL1 might interact with TRIM28 and repress the transcription of TEs at some stages of prenatal development, and that this CLOCK-independent activity of BMAL1 might contribute to the early aging phenotype of *Bmal1*$^{-/-}$ adult mice[9,10]. This idea agrees with emerging reports that indicate that the activity of retrotransposons is an important source of aging in metazoan organisms through the alteration of gene expression programmes and DNA

https://doi.org/10.1038/s41467-025-63778-4

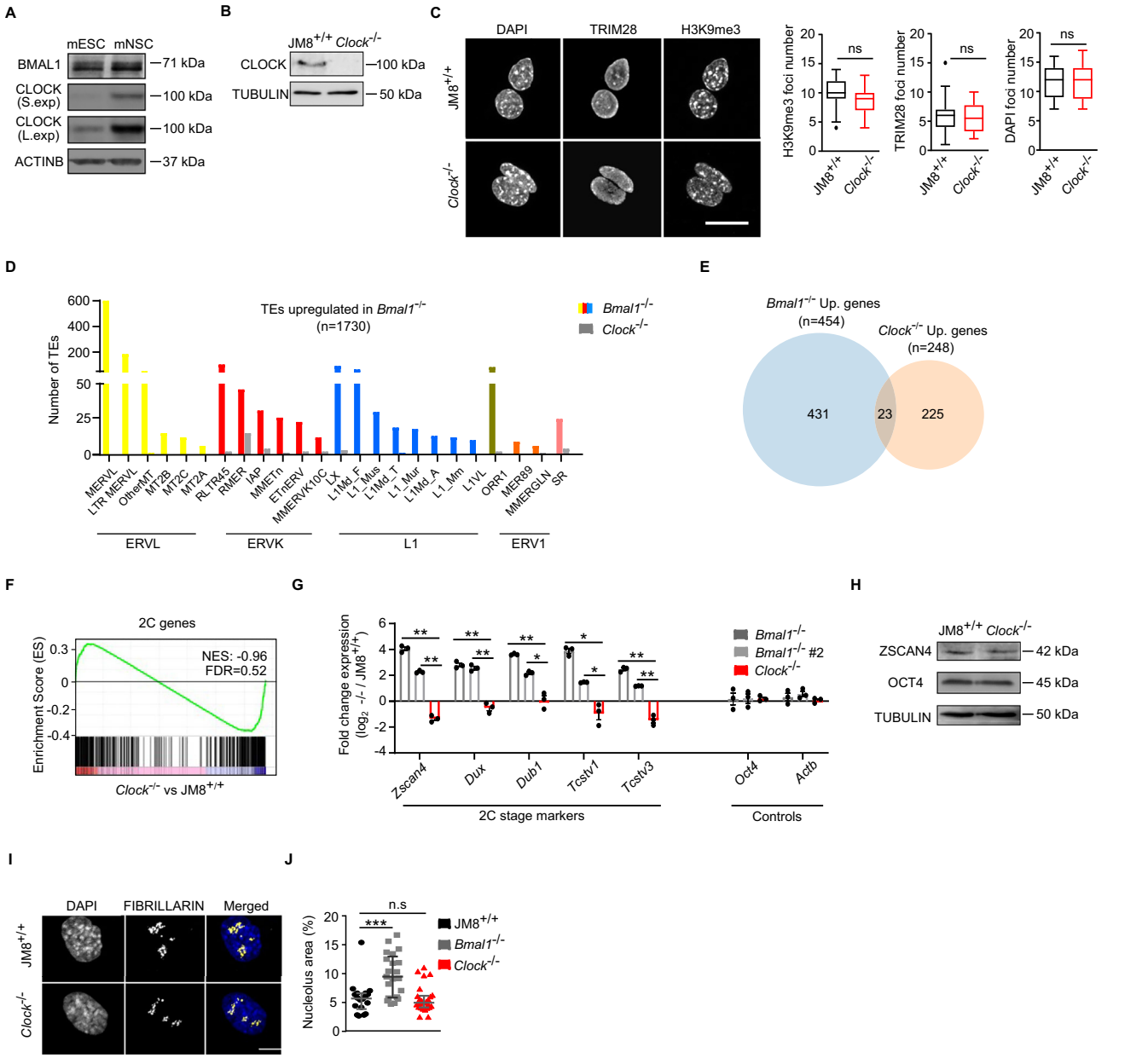

Fig. 5 | *Clock*$^{-/-}$ mESCs do not phenocopy *Bmal1*$^{-/-}$ mESCs. A Western blot analysis of whole cell extracts comparing the expression of BMAL1 and CLOCK in mESCs and mNSCs. Short (S. exp) and long (L. exp) exposures of the anti-CLOCK signal are presented. ACTINB was used as a loading control. **B** Western blot analysis of whole cell extracts measuring the level of CLOCK protein in JM8$^{+/+}$ and *Clock*$^{-/-}$ mESCs. TUBULIN is used as a loading control. **C** Immunofluorescence images of DAPI, TRIM28 and H3K9me3 labelling in JM8$^{+/+}$ and *Clock*$^{-/-}$ mESCs (left panel). Scale bar is 10 μm. Boxplots showing the number of DAPI, TRIM28 and H3K9me3 foci per nucleus ($n = 20$ per genotype) (right panels). n.s. indicates non-significant (two-tailed Mann–Whitney). Boxplots show median (line), IQR (box), whiskers to 1.5×IQR; outliers are individual points. **D** Histogram showing the number of TEs overexpressed in *Bmal1*$^{-/-}$ and *Clock*$^{-/-}$ mESCs and belong to indicated TE families. **E** Venn diagram showing the overlap between the genes upregulated (FC > 2, $p < 0.05$) in *Bmal1*$^{-/-}$ and in *Clock*$^{-/-}$ mESCs. **F** Gene Set Enrichment Analysis of 2C-associated genes in *Clock*$^{-/-}$ mESCs. Normalized Enrichment Score (NES) and FDR are indicated. **G** Gene expression analysis by RT-qPCR of 2C-associated genes in *Bmal1*$^{-/-}$, *Bmal1*$^{-/-}$#2 and *Clock*$^{-/-}$ relative to matched parental control mESCs. Expression was internally normalized against housekeeping genes (*Hmbs, Yhwaz*). Expression of *Oct4* and *Actb* genes were used as controls. Mean ± SEM of three experiments is shown. Asterisks indicate $p < 0.05$ in two-tailed Mann-Whitney test. (H) Western blot analysis of whole cells lysates comparing the expression of ZSCAN4 and OCT4 proteins in JM8$^{+/+}$ and Clock$^{-/-}$ mESCs. TUBULIN was used as a loading control. (I) Immunofluorescence images of the nucleolar protein FIBRILLARIN and DAPI staining in JM8$^{+/+}$ and *Clock*$^{-/-}$ mESCs. Scale bar is 10 μm. **J** Boxplot showing the percentage of the area of the nucleus that is occupied by FIBRILLARIN foci in JM8$^{+/+}$, *Bmal1*$^{-/-}$, and *Clock*$^{-/-}$ mESCs ($n = 30$ cells per genotype). Median and IQR are indicated. Asterisks indicate $p < 0.0001$ in two-tailed Mann-Whitney test. n.s. indicates non-significant differences. Two biological replicates were performed in **A**, **B** and **H**. Source data are provided as a Source Data file.

integrity[59,60]. However, it is also possible that the progeria-like syndrome of *Bmal1*$^{-/-}$ mice is also based on additional mechanisms that do not involve CLOCK nor TEs expression, because the BMAL1-interacting factors TRIM28 and RIF1, as well as H3K9me3, might regulate other aging-associated processes such as DNA repair and/or correct chromosome segregation[61–63]. Future research will need to dissect the molecular details as to how the function of BMAL1-TRIM28 during embryogenesis protects from premature aging during adulthood.

Methods

Cell culture and derivation of mESCs lines

JM8$^{+/+}$ (background C57BL6/N)-derived naïve mESCs were grown on 0.1% gelatin-coated dishes at 37 °C and 5% CO_2, and in N2B27 serum-free media containing Mitogen-Activated Protein Kinase (MEK) inhibitor PD0325901 (1 μM) (Millipore), Glycogen Synthase Kinase 3 (GSK3) inhibitor CHIR99021 (3 μM) (Millipore) and Leukaemia-Inhibitory Factor (LIF) as previously described[64] (2i+LIF media). Neural Stem Cells (NSCs) were derived from wild-type JM8 mESCs using a described protocol[65].

JM8-derived *Bmal1*$^{-/-}$ mESCs were previously described[16]. *Clock*-/- mESCs were derived from JM8$^{+/+}$ mESCs following a described protocol[16]. Briefly, the *Clock* gene was targeted by CRISPR/Cas9 on exon 6 using guide RNAs cloned in PX458, lipofectamine transfection followed by flow cytometry sorting and isolation of genetic clones. Genetic edition of targeted exon was analysed by PCR (oligos Supplementary Data 3) and Sanger sequencing, followed by the ICE CRISPR analysis tool (Synthego). The absence of CLOCK protein was checked by Western blot in clones harbouring nonsense mutations.

To derive JM8 cells that express two FLAG sequences in tandem (2XFLAG) on the N-terminus of BMAL1 protein, we obtained *Bmal1* cDNA from JM8 cells, fused it with a 2XFLAG sequence, cloned it into the pCAG-Puromycin expressing vector, and transfected it into cells to obtain genetically clonal populations of mESCs. Specifically, we isolated mRNA from JM8$^{+/+}$ cells using Trizol reagent (Thermofisher), reverse transcribed it using SuperScript III Reverse Transcriptase (Invitrogen) and specific primers against *Bmal1* mRNA. Forward primer (Supplementary Data 3) anneals on the second codon of *Bmal1* mRNA and includes an adapter stuffer sequence on 5′ end. Reverse primer (Supplementary Data 3) anneals on the stop codon of *Bmal1* and includes a NotI target sequence on the 3′ end. A 2XFLAG sequence containing a NotI restriction site on the 5′ and the stuffer sequence on the 3′ was amplified with KAPA Hifi HotStart Readymix (Kapa Byosystems) PCR system, using the pCAG-2XFLAG-JARID2-Puromycin plasmid as template[66], a forward primer with NotI adapter sequence (Supplementary Data 3) and a reverse primer annealing on the stuffer sequence (Supplementary Data 3). 2X*Flag:Bmal1* DNA molecules were generated by overlap extension PCR using the KAPA HiFi HotStart Readymix, the forward primer designed to amplify the 2XFLAG sequence and the reverse primer designed to amplify the Bmal1 cDNA. PCR fragment was digested using NotI (NEB) and ligated with NotI-digested pCAG-Puromycin plasmid using T4 DNA ligase (NEB) to generate the pCAG-2XFLAG-BMAL1 plasmid. Sequence fidelity of the 2X*Flag:Bmal1* transgene was confirmed by PCR followed by Sanger sequencing with multiple oligos covering all the open reading frame (Supplementary Data 3). JM8$^{+/+}$ mESCs were transfected with the pCAG-2XFLAG-BMAL1 plasmid using Lipofectamine 2000 and cells resistant to 0.3 μg/mL Puromycin were selected for 10 days. Resistant colonies were isolated and the expression of FLAG-BMAL1 was measured by western blot to select clones in which the level of expression of FLAG-BMAL1 and endogenous BMAL1 were similar.

Analysis of spontaneous differentiation towards trophectoderm

To measure spontaneous differentiation of JM8$^{+/+}$ and *Bmal1*$^{-/-}$ mESCs towards trophectoderm, cells were transferred to serum mESC media without MEK and GSK3 inhibitors as described previously[46]. Briefly, cells were plated at low density (100 cells/cm^2) and allowed to form colonies for ten days on 0.1% gelatin-coated dishes with DMEM KO (Gibco) media supplemented with 10% FBS (Gibco), LIF, penicillin/streptomycin (Gibco), L-glutamine (Gibco), 2-mercaptoethanol (Gibco).

RT-qPCR analysis

Total RNA was extracted using Trizol reagent (Thermofisher), digested with DNAseI (Invitrogene) and reverse transcribed using RevertAid First Strand cDNA synthesis kit (Thermofisher). For the analysis of expression of MERVL elements, the RNA was additionally digested with RQ1 DNAse (Promega) to guarantee the absence of contaminant genomic DNA. qPCR was carried out using GoTaq qPCR Master Mix with SYBR Green (Promega). Primers used are provided in Supplementary Data 3. Primers used for expression of pre-rRNA transcripts were described previously[67].

Immunofluorescence analysis

Immunofluorescence analysis was carried out as described previously[68]. Briefly, mESCs were fixed for 20 minutes in 2% paraformaldehyde, permeabilized 5 minutes in 0.4% Triton-X100 and blocked for 30 minutes in blocking buffer (PBS supplemented with 0.05% Tween 20, 2.5% bovine serum albumin and 10% goat serum). Detailed information on the primary antibodies used is included in Supplementary Data 3. Goat anti-mouse Alexa fluor 488 (Thermofisher, A-11001), goat anti-rabbit Alexa fluor 555 (Thermofisher, A-21429) were used as secondary antibodies. Vecta-shield mounting media with 1 μg/ml freshly added DAPI was used. Slides were analysed using a widefield fluorescence microscope, Zeiss Axio Imager and the ImageJ software.

Western blot analysis

Western blots of whole cell extracts, or histone preparations, were carried out as previously described[16]. Primary antibodies used are listed in Supplementary Data 3. A secondary species-specific antibodies conjugated to horseradish peroxidase was used (anti-rabbit-HRP, GE-Healthcare). Clarity Western ECL reagents (Bio-Rad) were used as chemiluminescent substrate. Anti-CLOCK and anti-BMAL1 western blot were developed with SuperSignal West Femto Maximum Sensitivity Substrate (Thermo Scientific).

Co-immunoprecipitation followed by western blot and mass spectrometry analysis

Two biological replicates of nuclear extracts of 4×10^7 FLAG-BMAL1 and JM8$^{+/+}$ cells were prepared as previously described[69]. Nuclear extracts were quantified with Bradford and 2 mg of lysate was mixed with 6 μg of antibody and 50 μL of Protein G magnetic beads (Dynabeads, Invitrogen) in 500 μl of buffer C (300 mM NaCl, 20 mM Hepes-KOH, pH 7.9, 20% v/v glycerol, 2 mM MgCl2, 0.2 mM EDTA, 0.1% NP-40, protease inhibitors, and 0.5 mM dithiothreitol) overnight. The reaction was washed 4 times: twice with buffer C and 0.5% NP-40, followed by one with PBS and 0.5% NP-40 and a final one with PBS. To perform western-blot analyses, immunoprecipitated proteins were eluted in 70 μl of NuPage loading buffer (final concentration of loading buffer 2X and 50 mM DTT) per IP at 70 °C for 15 min.

In Western blots, all immunoprecipitated material was loaded and compared to 1% or 10% of the input lysate. For mass spectrometry analysis, the magnetic beads used in immunoprecipitation were cleaned three times with 500 μl of 200 mM ammonium bicarbonate and 60 μl of 6 M Urea / 200 mM ammonium bicarbonate was added. Samples were then reduced with dithiothreitol (30 nmol, 37 °C, 60 min), alkylated in the dark with iodoacetamide (60 nmol, 25 °C, 30 min) and diluted to 1 M urea with 200 mM ammonium bicarbonate for trypsin digestion (1 μg, 37 °C, 8 h, Promega). After digestion, the peptide mix was acidified with formic acid and desalted with a MicroSpin C18 column (The Nest Group, Inc.) prior to LC-MS/MS analysis. The samples were then analysed using an LTQ-Orbitrap Fusion Lumos mass spectrometer (Thermo Fisher Scientific, San Jose, CA, USA) coupled to an EASY-nLC 1200 (Thermo Fisher Scientific, Proxeon, Odense, Denmark). Peptides were loaded directly onto the analytical column and were separated by reversed-phase chromatography using a 50-cm column with an inner diameter of 75 μm, packed with 2 μm C18 particles. Chromatographic gradients started at 95% buffer A and 5% buffer B with a flow rate of 300 nl/min and gradually increased to 25% buffer B and 75% A in 52 min and then to 40% buffer B

and 60% A in 8 min. After each analysis, the column was washed for 10 min with 100% buffer B. Buffer A: 0.1% formic acid in water. Buffer B: 0.1% formic acid in 80% acetonitrile. The mass spectrometer was operated in positive ionization mode with nanospray voltage set at 2.4 kV and source temperature at 305 °C. The acquisition was performed in data-dependent acquisition (DDA) mode and full MS scans with 1 micro scans at a resolution of 120,000 were used over a mass range of m/z 350–1400 with detection in the Orbitrap mass analyser. Auto gain control (AGC) was set to 'standard' and injection time to 'auto'. In each cycle of data-dependent acquisition analysis, following each survey scan, the most intense ions above a threshold ion count of 10,000 were selected for fragmentation. The number of selected precursor ions for fragmentation was determined by the "Top Speed" acquisition algorithm and a dynamic exclusion of 60 seconds. Fragment ion spectra were produced via high-energy collision dissociation (HCD) at a normalized collision energy of 28% and they were acquired in the ion trap mass analyzer. AGC and injection time were set to 'Standard' and 'Dynamic', respectively and an isolation window of 1.4 m/z was used. Digested bovine serum albumin (New England Biolabs) was analysed between each sample to avoid sample carryover and to assure stability of the instrument. QCloud has been used to control instrument longitudinal performance during the project.

Acquired spectra were analysed using the Proteome Discoverer software suite (v1.4, Thermo Fisher Scientific) and the Mascot search engine (v2.6, Matrix Science). Data was analysed against a Swiss-Prot mouse database (as in March 2021, 17082 entries) plus a list of common contaminants and all the corresponding decoy entries. For peptide identification, a precursor ion mass tolerance of 7 ppm was used for the MS1 level, trypsin was chosen as the enzyme and up to three missed cleavages were allowed. The fragment ion mass tolerance was set to 0.5 Da for MS2 spectra. Oxidation of methionine and N-terminal protein acetylation were used as variable modifications, whereas carbamidomethylation on cysteines was set as a fixed modification. False discovery rate (FDR) in peptide identification was set to a maximum of 5%. We used SAINT to establish significant interactors of BMAL1, comparing biological duplicates of FLAG-BMAL1 and JM8$^{+/+}$ cells. We detected 815 interacting proteins. We found 228 interactors with a fold change (Flag-Bmal1/JM8) higher than 30 and with a Bayesian false discovery rate (BFDR) lower than 0.05. STRING software was used to identify the cluster of 25 proteins involved in transcriptional regulation with a BFDR of zero.

Calibrated chromatin immunoprecipitation sequencing (cChIP-seq) and data analysis

cChIP-seq using spike-in cells was carried out as previously described[70] with some modifications. Briefly, cells were trypsinized, resuspended in mESCs cell-culture media and counted. mESCs cells were mixed with human A549 cells in a proportion of 25:1 as spike-in control per reaction. Four million JM8$^{+/+}$ or *Bmal1*$^{-/-}$ mESCs were used for each cChIP-seq reaction. Ten million cells were used as starting material in the FLAG-BMAL1 ChIP-seq that did not require calibration. Cells were spined and resuspended in 37 °C complete media at a density of 5×10^6 cells/ml and incubated in a rotating platform for 12 min with 1% formaldehyde at room temperature. After quenching formaldehyde fixation with glycine (125 mM final concentration), cells were resuspended in swelling buffer (25 mM HEPES pH 7.9, 1.5 mM MgCl2, 10 mM KCl, 0.1% NP-40) at a density of 2.5×10^6 cells/ml. Nuclei were isolated using a Dounce homogenizer (tight pestle; 50 strokes). Nuclei were resuspended in sonication buffer (1×10^7 cells/ml) and sonicated 1:30 h at full power, 4 °C (30 sec ON /30 sec Off). Primary antibodies (Supplementary Data 3) were added to chromatin and incubated in a rotating wheel at 4 °C overnight. Protein G magnetic beads (Dynabeads, Invitrogen) were added, and chromatin was incubated for 5 hours. Washes were carried out for 5 min at 4 °C with 1 ml of the following buffers: 1× sonication buffer, 1× wash buffer A (50 mM Hepes (pH 7.9), 500 mM NaCl, 1 mM EDTA, 1% Triton X-100, 0.1% Na-deoxycholate, and 0.1% SDS), 1× wash buffer B (20 mM tris (pH 8.0), 1 mM EDTA, 250 mM LiCl, 0.5% NP-40, and 0.5% Na-deoxycholate), and 2× TE buffer (pH 8). DNA was eluted in elution buffer (50 mM Tris, pH 7.5, 1 mM EDTA, 1% SDS) and reversed cross-linked overnight at 65 °C in 160 mM NaCl and 20 μg/ml RNase, followed by 2 h 45 °C incubation with proteinase K (220 μg/ml).

Libraries of immunoprecipitated DNA were generated from 3 ng of starting DNA with the NEBNext Ultra DNA Library Prep kit for Illumina (New England Biolabs) according to manufacturer's instructions at the CRG Genomics Core Facility (Barcelona) and sequenced using a NextSeq 500 Illumina technology. 20–30 million reads (75 bp paired-end reads) were obtained for each library.

The quality of libraries was evaluated using FastQC v0.11.5 software. Reads were aligned using Bowtie2[71] to the genome sequence of the concatenated mouse (mm10) and spike-in genomes (hg19) using the "–no-mixed" and "–no-discordant" options. Unique-mapping and multi-hit reads were kept using Bowtie2. Multi-hit reads were allocated only to one genomic region with the highest alignment score[72]. Duplicates were then removed and the alignments to the mouse genome were separated from the human spike-in. The mouse reads were sorted and indexed using SAMTools and sambamba[73,74]. Mouse reads were then randomly subsampled using the calculated down-sampling factor for each ChIP using a random seed of 123. Down sampling factor was calculated for each sample, considering the ratio of sequences aligned to the inputs of the spike-in and the mouse genome, as well as the number of reads aligning to the spike-in of each ChIP sample. BigWigs were generated using the deepTools suite[75] without further normalization for calibrated samples and with reads per kilobase per million (RPKM) for uncalibrated ones. Peak calling was performed with MACS3[76] using FDR < 0.05 as a threshold. The genome location of detected peaks was classified using HOMER[77].

Read coverage of the cChIP-seqs was calculated with the R-package CoverageView version 1.38.0. with no further normalization. FLAG-BMAL1 non-calibrated ChIP-seq coverage plots were measured as reads per million (RPM). TRIM28 peaks with average read signal above the 95th percentile or below the 5th percentile were discarded, and the average read signal around the centre of the remaining peaks was plotted. Binning of 10 bp was used. Read coverage of upregulated MERVLs or solo LTR sequences was calculated by dividing the DNA sequence of each element into 100 windows, calculating the average reads of each window, and plotting the average value of all elements per window. Average read coverage around the TSS of annotated genes was calculated. To analyse the read coverage in contiguous genomic intervals, the genome sequence was divided in contiguous windows of 1000 bps and the total reads mapping to these windows were calculated. The sum of ten consecutive 1000 bp windows was calculated for TRIM28, BMAL1 and FLAG-BMAL1 ChIP-seqs, while the sum of 100 consecutive 1000 bp windows was used to analyse H3K9me3 distribution. These values were used to generate correlation plots and histograms with the number of windows. Coverage values for H3K9me3 cChIP-seq were normalized by subtracting input signals.

Reads signal along the consensus sequences of MERVLs and LTRs was obtained by aligning reads to the consensus sequences retrieved from RepBase (www.girinst.org/repbase/) using Samtools[73]. The average coverage of consensus sequences from different families of TEs was calculated. The fold change between JM8$^{+/+}$ and Bmal1$^{-/-}$ was calculated and plotted as red-white heatmap.

Domain calling was performed with SICER2[78] using -w 800 -g 2400 -f 150 -fdr 0.05 options. ChIP-qPCR analysis was performed using GoTaq qPCR Master Mix (Promega) in a QuantStudio™ 3 Real Time PCR system (Applied Biosystems) using primers detailed in Supplementary Data 2. Enrichment was calculated relative to 1% input.

mRNA sequencing and data analysis

Biological replicates of total RNA from 2×10^5 JM8$^{+/+}$ and *Clock*$^{-/-}$ mESCs growing in 2i + LIF media using Trizol reagent (Thermofisher) were obtained. mRNA library preparation using TruSeq Stranded mRNA kit (Illumina) and Illumina sequencing (30 million reads, 75-bp paired end) was carried out at the National Centre for Genomic Analysis - Centre for Genomic Regulation (CNAG-CRG). Datasets of published mRNA-seq comparing JM8$^{+/+}$ and *Bmal1*$^{-/-}$ mESCs[16] were included in downstream analyses.

Quality of mRNAseq libraries was evaluated using FastQC v0.11.5 software[79]. RNA paired-end reads were aligned to mm10 mouse genome assembly with STAR v2.5.3a[80] and quantified with featureCounts v2.0.1[81] using Gencode vM22 annotation. Differentially expressed genes were determined with the R package DESeq2 v1.36[82]. Shrinkage of effect size was performed on DESeq2 results using the apeglm method through the function lfcShrink. Gene Set Enrichment Analysis (GSEA) was performed with the GSEA software from the Broad Institute and UC San Diego[83]. The set of genes expressed in embryos during the 2-cell stage and used in GSEA analyses was obtained from previous studies[84].

Analysis of the expression of transposable elements

For Transposable Elements (TE) expression analysis, the SQuIRE v0.9.9.92 pipeline[85] was used to count transposable elements expression following default parameters. Code was modified to include simple repeats, satellites, and low complexity regions in this analysis. TE differential expression analysis was performed from SQuIRE counts using DESeq2 as previously stated. mm10 repeat annotation (RepeatMasker) was downloaded from the UCSC table browser.

Analysis of the expression of different of MERVL elements in *Bmal1*$^{-/-}$ mESCs was performed by calculating the fold change expression relative to JM8$^{+/+}$ cells in group of elements described elsewhere[86]. Briefly, the MERVL-int (>5 kb) elements flanked by two MT2_Mm or MT2C_Mm were categorized as full-length elements. Additionally, MT2 and MERVL-int were required to be in the same strand, and the total length (2xMT2+int) should be <10 kb. MT2 copies lacking nearby MERVL-int (>5 kb) were classified as solo MT2. The remaining copies were defined as other MERVL copies.

Identification of the nearest protein-coding genes annotated around the TEs that are differentially expressed in *Bmal1*$^{-/-}$ mESCs was achieved by using the annotatePeakInBatch function in the ChIPpeakAnno R package[87].

The mRNA-seq reads were aligned to the consensus sequences of different TE subfamilies with Bowtie2[71] using the --no-unal option. The total number of alignments was obtained with Samtools[73] and normalized to the total number of reads aligned to the reference genome. Reads per million and $\log_2$ fold-change values between *Bmal1*$^{-/-}$ and JM8$^{+/+}$ were calculated.

Quantification of chimeric transcripts was performed using ChimeraTE[88]. Chimeric transcripts formed by elements annotated in the reference genome were detected using ChimeraTE mode 1, considering only genes with TE copies located 5 kb upstream or downstream. A genome-blind approach was additionally performed using ChimeraTE mode 2 to detect chimeras from fixed and polymorphic TEs without the reference genome. Reference genome, reference transcripts and gene annotations files were obtained from GENCODE assembly GRCm38.p6 (mm10). TE annotations and TE reference transcripts in the mouse genome (RepeatMasker 4.0) were downloaded from UCSC web page.

MERVL elements overexpressed in *Bmal1*$^{-/-}$ cells relative to parental cells were classified as self-dependent (intergenic or within a gene that is not overexpressed in *Bmal1*$^{-/-}$ cells) or gene-dependent (within a gene that is overexpressed (FC > 2, $p < 0.05$) in *Bmal1*$^{-/-}$ cells) was carried out described previously[89] with some modifications. To annotate the position of induced TEs relative to genes (mm10 annotations from the NCBI RefSeq database downloaded from UCSC Table Browser[90]), the R package ChIPpeakAnno[87] was used with the following genomic priority: 5′ UTR > 3′ UTR > Exon > Intron > Intergenic. In addition, TEs that fall within a gene that is not expressed in either JM8$^{+/+}$ nor *Bmal1*$^{-/-}$ cells were considered as self-dependent.

Karyotype-like analysis of the genome-wide distribution of deregulated genes and MERVL elements was performed using karyoploteR[91].

Analysis of mRNA alternative splicing variants

Analysis of mRNA alternative splicing variants was performed in *Bmal1*$^{-/-}$ (relative to parental JM8$^{+/+}$ cells). A previously described positive control was used (shZfp207 versus parental control mESCs[92]). Mouse genomic sequences (mm10) and gene annotations (refSeq) were retrieved from the UCSC genome browser. Mappings to the mouse genome were carried out with STAR v2.7.3[80] using the SQUIRE[85] optimized parameters (--outFilterMultimapNmax 500 --winAnchorMultimapNmax 500 --alignEndsProtrude 100 DiscordantPair --outFilterScoreMinOverLread 0.4 --outFilterMatchNminOverLread 0.4 --chimSegmentMin 17 --alignIntronMax 300000 --outSAMattrIHstart 0). rMAts v4.1.1[93] was used for alternative splicing analyses with options (--allow-clipping --variable-read-length --readLength 100 -t paired) and results were gathered (FDR < 0.05) for 5 classes of events: SE, MXE, A5SS, A3SS and RI.

Chromosome conformation capture analyses by Hi-C

Hi-C was performed as previously described[94] with minor modifications. In brief, 4×10^6 JM8$^{+/+}$ and *Bmal1*$^{-/-}$ cells were fixed with formaldehyde 1% and digested overnight at 37 °C using 400U of MboI (New England Biolabs, #R0147M). After filling with 50 nM biotin-dATP (Invitrogen, #10484552) and 50U of Klenow polymerase (New England Biolabs, #M0210M), proximity ligation was carried out overnight at 16 °C with 10000U of T4 DNA Ligase (New England Biolabs, #M0202M). Chromatin was reverse-crosslinked with 16U of Proteinase K (New England Biolabs, #P8107S) and 100 ug RNAase A (Thermo Scientific, #EN0531), and DNA was purified using AMPure XP beads (Beckman Coulter, #A63881) and sonicated using Sonicator Bioruptor PICO (Diagenode) to produce fragments of 300-400 bp. Sonicated fragments containing biotin were immobilized on MyOne Streptavidin T1 beads (Invitrogen, #65601), end-repaired with the NEBNext End Repair Module (New England Biolabs, #E6050L) and A-tailed with the NEBNext dA-Tailing Module (New England Biolabs, #E6053L). After adapters ligation, libraries were indexed and amplified with NEBNext UDI primer pairs (New England Biolabs, #E6440S) during 8 PCR cycles with NEBNext HiFi PCR Master mix (New England Biolabs, #M0541S). Fragments of DNA 300 and 800 bp were then selected using AMPure XP beads (Beckman Coulter, #A63881). Sequencing was performed at the National Centre for Genomic Analysis (CNAG) using NovaSeq 6000 technology and sequencing >400 millions of 150 bp PE reads per sample.

Hi-C datasets were processed using TADbit[95]. Specifically, for both JM8$^{+/+}$ and *Bmal1*$^{-/-}$ cells, paired-end FASTQ files of 2 Hi-C replicates, previously assessed for reproducibility[96], were merged and mapped to the mouse GRCm38/mm10 reference genome applying a fragment-based iterative strategy[97] using the GEM mapper[98]. Mapped reads were filtered using TADbit with default parameters, which removed self-circles, dangling ends, duplicated and random breaks, among other minor artefactual reads[95]. After mapping and filtering, the resulting Hi-C matrices contained a total of 505,149,739 valid pairs for JM8$^{+/+}$ and 285,113,464 for *Bmal1*$^{-/-}$ mutant cells. The resulting raw Hi-C interaction matrices were next normalized with ICE balancing[97] at the resolutions of 10 kb, 50Kb, 100Kb, 500Kb, and 1 Mb.

Compartment analysis was performed on observed-over-expected contact maps at resolutions equivalent to 20 kb, 50 kb, and 100 kb bins using the *cooltools eigs-cis* module[99]. Active (A) and

inactive (B) compartment types were assigned by GC-content. Saddle plots were generated using the *cooltools saddle* module. Compartment strength was calculated as the ratio of homotypic (AA + BB) over heterotypic (AB + BA) compartment contacts. The top 20% of observed/expected values for both homotypic and heterotypic interactions were chosen. Insulation scores were calculated using *cooltools* insulation module at resolution of 50 kb, which identified boundaries categorized into strong and weak as implemented in the module.

General

R version 4.2.2 and R-studio version 2023.6.1.524 were used. Results were plotted with the ggplot2 package version 3.4.2. GraphPad Prism9 was used for statistical analysis and data presentation.

Reporting summary

Further information on research design is available in the Nature Portfolio Reporting Summary linked to this article.

Data availability

Datasets are available at GEO-NCBI with accession number GSE263285. Raw proteomics data has been deposited in PRIDE repository with identifier PXD050769. Source data are provided with this paper.

References

1. Dibner, C., Schibler, U. & Albrecht, U. The mammalian circadian timing system: organization and coordination of central and peripheral clocks. *Annu. Rev. Physiol.* **72**, 517–549 (2010).
2. Mohawk, J. A., Green, C. B. & Takahashi, J. S. Central and peripheral circadian clocks in mammals. *Annu. Rev. Neurosci.* **35**, 445–462 (2012).
3. Takahashi, J. S. Transcriptional architecture of the mammalian circadian clock. *Nat. Rev. Genet.* **18**, 164–179 (2017).
4. Zhang, R., Lahens, N. F., Ballance, H. I., Hughes, M. E. & Hogenesch, J. B. A circadian gene expression atlas in mammals: implications for biology and medicine. *Proc. Natl Acad. Sci. USA* **111**, 16219–16224 (2014).
5. Turek, F. W. Circadian clocks: Not your grandfather's clock. *Science* **354**, 992–993 (2016).
6. Roenneberg, T. & Merrow, M. The Circadian Clock and Human Health. *Curr. Biol.: CB* **26**, R432–R443 (2016).
7. Bass, J. & Lazar, M. A. Circadian time signatures of fitness and disease. *Science* **354**, 994–999 (2016).
8. Turek, F. W. et al. Obesity and metabolic syndrome in circadian Clock mutant mice. *Science* **308**, 1043–1045 (2005).
9. Kondratov, R. V., Kondratova, A. A., Gorbacheva, V. Y., Vykhovanets, O. V. & Antoch, M. P. Early aging and age-related pathologies in mice deficient in BMAL1, the core componentof the circadian clock. *Genes Dev.* **20**, 1868–1873 (2006).
10. Yang, G. et al. Timing of expression of the core clock gene Bmal1 influences its effects on aging and survival. *Sci. Transl. Med.* **8**, 324ra316 (2016).
11. Amano, T. et al. Expression and functional analyses of circadian genes in mouse oocytes and preimplantation embryos: Cry1 is involved in the meiotic process independently of circadian clock regulation. *Biol. Reprod.* **80**, 473–483 (2009).
12. Alvarez, J. D., Chen, D., Storer, E. & Sehgal, A. Non-cyclic and developmental stage-specific expression of circadian clock proteins during murine spermatogenesis. *Biol. Reprod.* **69**, 81–91 (2003).
13. Morse, D., Cermakian, N., Brancorsini, S., Parvinen, M. & Sassone-Corsi, P. No circadian rhythms in testis: Period1 expression is clock independent and developmentally regulated in the mouse. *Mol. Endocrinol. (Baltim., Md)* **17**, 141–151 (2003).
14. Yagita, K. et al. Development of the circadian oscillator during differentiation of mouse embryonic stem cells in vitro. *Proc. Natl Acad. Sci. USA* **107**, 3846–3851 (2010).
15. Kowalska, E., Moriggi, E., Bauer, C., Dibner, C. & Brown, S. A. The circadian clock starts ticking at a developmentally early stage. *J. Biol. Rhythms* **25**, 442–449 (2010).
16. Gallardo A. et al. The molecular clock protein Bmal1 regulates cell differentiation in mouse embryonic stem cells. *Life Sci. Alliance* **3**, (2020).
17. Ameneiro C. et al. BMAL1 coordinates energy metabolism and differentiation of pluripotent stem cells. *Life Sci. Alliance* **3**, (2020).
18. Umemura, Y. et al. Involvement of posttranscriptional regulation of Clock in the emergence of circadian clock oscillation during mouse development. *Proc. Natl Acad. Sci. USA* **114**, E7479–e7488 (2017).
19. Schulz, K. N. & Harrison, M. M. Mechanisms regulating zygotic genome activation. *Nat. Rev. Genet.* **20**, 221–234 (2019).
20. Riveiro, A. R. & Brickman, J. M. From pluripotency to totipotency: an experimentalist's guide to cellular potency. *Development* **147**, dev189845 (2020).
21. Genet, M. & Torres-Padilla, M. E. The molecular and cellular features of 2-cell-like cells: a reference guide. *Development* **147**, dev189688 (2020).
22. Nichols, J. & Smith, A. Pluripotency in the embryo and in culture. *Cold Spring Harb. Perspect. Biol.* **4**, a008128 (2012).
23. Macfarlan, T. S. et al. Embryonic stem cell potency fluctuates with endogenous retrovirus activity. *Nature* **487**, 57–63 (2012).
24. Ecco, G., Imbeault, M. & Trono, D. KRAB zinc finger proteins. *Development* **144**, 2719–2729 (2017).
25. Korutla, L., Degnan, R., Wang, P. & Mackler, S. A. NAC1, a cocaine-regulated POZ/BTB protein interacts with CoREST. *J. Neurochemistry***101**, 611–618 (2007).
26. Li, P. et al. Rif1 promotes a repressive chromatin state to safeguard against endogenous retrovirus activation. *Nucleic Acids Res.* **45**, 12723–12738 (2017).
27. Schultz, D. C., Friedman, J. R. & Rauscher, F. J. 3rd. Targeting histone deacetylase complexes via KRAB-zinc finger proteins: the PHD and bromodomains of KAP-1 form a cooperative unit that recruits a novel isoform of the Mi-2alpha subunit of NuRD. *Genes Dev.* **15**, 428–443 (2001).
28. Schultz, D. C. et al. SETDB1: a novel KAP-1-associated histone H3, lysine 9-specific methyltransferase that contributes to HP1-mediated silencing of euchromatic genes by KRAB zinc-finger proteins. *Genes Dev.* **16**, 919–932 (2002).
29. Quenneville, S. et al. The KRAB-ZFP/KAP1 system contributes to the early embryonic establishment of site-specific DNA methylation patterns maintained during development. *Cell Rep.* **2**, 766–773 (2012).
30. Grassi, D. A., Jönsson, M. E., Brattås, P. L. & Jakobsson, J. TRIM28 and the control of transposable elements in the brain. *Brain Res* **1705**, 43–47 (2019).
31. Matsui, T. et al. Proviral silencing in embryonic stem cells requires the histone methyltransferase ESET. *Nature* **464**, 927–931 (2010).
32. Rowe, H. M. et al. KAP1 controls endogenous retroviruses in embryonic stem cells. *Nature* **463**, 237–240 (2010).
33. Fueyo, R., Judd, J., Feschotte, C. & Wysocka, J. Roles of transposable elements in the regulation of mammalian transcription. *Nat. Rev. Mol. Cell Biol.* **23**, 481–497 (2022).
34. Peaston, A. E. et al. Retrotransposons regulate host genes in mouse oocytes and preimplantation embryos. *Dev. Cell* **7**, 597–606 (2004).
35. Sakashita, A. et al. Transcription of MERVL retrotransposons is required for preimplantation embryo development. *Nat. Genet.* **55**, 484–495 (2023).
36. Kruse K. et al. Transposable elements drive reorganisation of 3D chromatin during early embryogenesis. *bioRxiv*, 523712 (2019).
37. Dekker, J., Rippe, K., Dekker, M. & Kleckner, N. Capturing chromosome conformation. *Science* **295**, 1306–1311 (2002).

38. Lieberman-Aiden, E. et al. Comprehensive mapping of long-range interactions reveals folding principles of the human genome. *Science* **326**, 289–293 (2009).
39. Falco, G. et al. Zscan4: a novel gene expressed exclusively in late 2-cell embryos and embryonic stem cells. *Dev. Biol.* **307**, 539–550 (2007).
40. Kigami, D., Minami, N., Takayama, H. & Imai, H. MuERV-L is one of the earliest transcribed genes in mouse one-cell embryos. *Biol. Reprod.* **68**, 651–654 (2003).
41. Xie, S. Q. et al. Nucleolar-based Dux repression is essential for embryonic two-cell stage exit. *Genes Dev.* **36**, 331–347 (2022).
42. Dan, J. et al. Rif1 maintains telomere length homeostasis of ESCs by mediating heterochromatin silencing. *Dev. Cell* **29**, 7–19 (2014).
43. Zhang, W. et al. Rif1 and Hmgn3 regulate the conversion of murine trophoblast stem cells. *Cell Rep.* **38**, 110570 (2022).
44. Bilodeau, S., Kagey, M. H., Frampton, G. M., Rahl, P. B. & Young, R. A. SetDB1 contributes to repression of genes encoding developmental regulators and maintenance of ES cell state. *Genes Dev.* **23**, 2484–2489 (2009).
45. Yuan, P. et al. Eset partners with Oct4 to restrict extraembryonic trophoblast lineage potential in embryonic stem cells. *Genes Dev.* **23**, 2507–2520 (2009).
46. Wu, K. et al. SETDB1-mediated cell fate transition between 2C-Like and Pluripotent states. *Cell Rep.* **30**, 25–36.e26 (2020).
47. Cammas, F. et al. Mice lacking the transcriptional corepressor TIF1beta are defective in early postimplantation development. *Development* **127**, 2955–2963 (2000).
48. Hu, G. et al. A genome-wide RNAi screen identifies a new transcriptional module required for self-renewal. *Genes Dev.* **23**, 837–848 (2009).
49. Dodge, J. E., Kang, Y. K., Beppu, H., Lei, H. & Li, E. Histone H3-K9 methyltransferase ESET is essential for early development. *Mol. Cell. Biol.* **24**, 2478–2486 (2004).
50. Percharde, M. et al. A LINE1-Nucleolin Partnership Regulates Early Development and ESC Identity. *Cell* **174**, 391–405.e319 (2018).
51. Sun, X. et al. POGZ suppresses 2C transcriptional program and retrotransposable elements. *Cell Rep.* **42**, 112867 (2023).
52. Huang, N. et al. Crystal structure of the heterodimeric CLOCK:-BMAL1 transcriptional activator complex. *Science* **337**, 189–194 (2012).
53. de la Rosa, S., Del Mar Rigual, M., Vargiu, P., Ortega, S. & Djouder, N. Endogenous retroviruses shape pluripotency specification in mouse embryos. *Sci. Adv.* **10**, eadk9394 (2024).
54. Ke, Y. et al. 3D Chromatin structures of mature gametes and structural reprogramming during mammalian embryogenesis. *Cell* **170**, 367–381.e320 (2017).
55. Flyamer, I. M. et al. Single-nucleus Hi-C reveals unique chromatin reorganization at oocyte-to-zygote transition. *Nature* **544**, 110–114 (2017).
56. Du, Z. et al. Allelic reprogramming of 3D chromatin architecture during early mammalian development. *Nature* **547**, 232–235 (2017).
57. Fu, X., Djekidel, M. N. & Zhang, Y. A transcriptional roadmap for 2C-like-to-pluripotent state transition. *Sci. Adv.* **6**, eaay5181 (2020).
58. Liang, C. et al. BMAL1 moonlighting as a gatekeeper for LINE1 repression and cellular senescence in primates. *Nucleic Acids Res.* **50**, 3323–3347 (2022).
59. López-Otín, C., Blasco, M. A., Partridge, L., Serrano, M. & Kroemer, G. Hallmarks of aging: An expanding universe. *Cell* **186**, 243–278 (2023).
60. Gorbunova, V. et al. The role of retrotransposable elements in ageing and age-associated diseases. *Nature* **596**, 43–53 (2021).
61. Ziv, Y. et al. Chromatin relaxation in response to DNA double-strand breaks is modulated by a novel ATM- and KAP-1 dependent pathway. *Nat. Cell Biol.* **8**, 870–876 (2006).
62. Janssen, A., Colmenares, S. U. & Karpen, G. H. Heterochromatin: Guardian of the Genome. *Annu. Rev. Cell Dev. Biol.* **34**, 265–288 (2018).
63. Buonomo, S. B., Wu, Y., Ferguson, D. & de Lange, T. Mammalian Rif1 contributes to replication stress survival and homology-directed repair. *J. Cell Biol.* **187**, 385–398 (2009).
64. Ying, Q. L. et al. The ground state of embryonic stem cell self-renewal. *Nature* **453**, 519–523 (2008).
65. Conti, L. et al. Niche-independent symmetrical self-renewal of a mammalian tissue stem cell. *PLoS Biol.* **3**, e283 (2005).
66. Landeira, D. et al. Jarid2 is a PRC2 component in embryonic stem cells required for multi-lineage differentiation and recruitment of PRC1 and RNA Polymerase II to developmental regulators. *Nat. Cell Biol.* **12**, 618–624 (2010).
67. Cervantes, M. et al. BMAL1 Associates with NOP58 in the Nucleolus and Contributes to Pre-rRNA Processing. *iScience* **23**, 101151 (2020).
68. Landeira, D. et al. Jarid2 coordinates Nanog Expression and PCP/Wnt signaling required for efficient ESC differentiation and early embryo development. *Cell Rep.* **12**, 573–586 (2015).
69. Kloet, S. L. et al. The dynamic interactome and genomic targets of Polycomb complexes during stem-cell differentiation. *Nat. Struct. Mol. Biol.* **23**, 682–690 (2016).
70. Gallardo, A. et al. EZH2 endorses cell plasticity to non-small cell lung cancer cells facilitating mesenchymal to epithelial transition and tumour colonization. *Oncogene* **41**, 3611–3624 (2022).
71. Langmead, B. & Salzberg, S. L. Fast gapped-read alignment with Bowtie 2. *Nat. Methods* **9**, 357–359 (2012).
72. Teissandier, A., Servant, N., Barillot, E. & Bourc'his, D. Tools and best practices for retrotransposon analysis using high-throughput sequencing data. *Mob. DNA* **10**, 52 (2019).
73. Tarasov, A., Vilella, A. J., Cuppen, E., Nijman, I. J. & Prins, P. Sambamba: fast processing of NGS alignment formats. *Bioinformatics* **31**, 2032–2034 (2015).
74. Li, H. et al. The sequence alignment/Map format and SAMtools. *Bioinformatics* **25**, 2078–2079 (2009).
75. Ramírez, F., Dündar, F., Diehl, S., Grüning, B. A. & Manke, T. deepTools: a flexible platform for exploring deep-sequencing data. *Nucleic Acids Res.* **42**, W187–W191 (2014).
76. Zhang, Y. et al. Model-based analysis of ChIP-Seq (MACS). *Genome Biol.* **9**, R137 (2008).
77. Heinz, S. et al. Simple combinations of lineage-determining transcription factors prime cis-regulatory elements required for macrophage and B cell identities. *Mol. Cell* **38**, 576–589 (2010).
78. Zang, C. et al. A clustering approach for identification of enriched domains from histone modification ChIP-Seq data. *Bioinformatics* **25**, 1952–1958 (2009).
79. Andrews S. FastQC: a quality control tool for high throughput sequence data). Babraham Bioinformatics, Babraham Institute, Cambridge, UK (2010).
80. Dobin, A. & Gingeras, T. R. Mapping RNA-seq Reads with STAR. *Curr. Protoc. Bioinforma.* **51**, 11.14.11–11.14.19 (2015).
81. Liao, Y., Smyth, G. K. & Shi, W. featureCounts: an efficient general purpose program for assigning sequence reads to genomic features. *Bioinformatics* **30**, 923–930 (2014).
82. Love, M. I., Huber, W. & Anders, S. Moderated estimation of fold change and dispersion for RNA-seq data with DESeq2. *Genome Biol.* **15**, 550 (2014).
83. Subramanian, A. et al. Gene set enrichment analysis: a knowledge-based approach for interpreting genome-wide expression profiles. *Proc. Natl Acad. Sci. USA* **102**, 15545–15550 (2005).
84. Deng, Q., Ramskold, D., Reinius, B. & Sandberg, R. Single-cell RNA-seq reveals dynamic, random monoallelic gene expression in mammalian cells. *Science* **343**, 193–196 (2014).

85. Yang, W. R., Ardeljan, D., Pacyna, C. N., Payer, L. M. & Burns, K. H. SQuIRE reveals locus-specific regulation of interspersed repeat expression. *Nucleic Acids Res.* **47**, e27 (2019).
86. Yang, J., Cook, L. & Chen, Z. Systematic evaluation of retroviral LTRs as cis-regulatory elements in mouse embryos. *Cell Rep.* **43**, 113775 (2024).
87. Zhu, L. J. et al. ChIPpeakAnno: a Bioconductor package to annotate ChIP-seq and ChIP-chip data. *BMC Bioinforma.* **11**, 237 (2010).
88. Oliveira, D. S. et al. ChimeraTE: a pipeline to detect chimeric transcripts derived from genes and transposable elements. *Nucleic Acids Res.* **51**, 9764–9784 (2023).
89. Chang, N. C., Rovira, Q., Wells, J., Feschotte, C. & Vaquerizas, J. M. Zebrafish transposable elements show extensive diversification in age, genomic distribution, and developmental expression. *Genome Res.* **32**, 1408–1423 (2022).
90. O'Leary, N. A. et al. Reference sequence (RefSeq) database at NCBI: current status, taxonomic expansion, and functional annotation. *Nucleic Acids Res.* **44**, D733–D745 (2016).
91. Gel, B. & Serra, E. karyoploteR: an R/Bioconductor package to plot customizable genomes displaying arbitrary data. *Bioinformatics* **33**, 3088–3090 (2017).
92. Malla, S. et al. ZFP207 sustains pluripotency by coordinating OCT4 stability, alternative splicing and RNA export. *EMBO Rep.* **23**, e53191 (2022).
93. Shen, S. et al. rMATS: robust and flexible detection of differential alternative splicing from replicate RNA-Seq data. *Proc. Natl Acad. Sci. USA* **111**, E5593–E5601 (2014).
94. Rao, S. S. et al. A 3D map of the human genome at kilobase resolution reveals principles of chromatin looping. *Cell* **159**, 1665–1680 (2014).
95. Serra, F. et al. Automatic analysis and 3D-modelling of Hi-C data using TADbit reveals structural features of the fly chromatin colors. *PLoS Comput. Biol.* **13**, e1005665 (2017).
96. Bonev, B. et al. Multiscale 3D Genome Rewiring during Mouse Neural Development. *Cell* **171**, 557–572.e524 (2017).
97. Imakaev, M. et al. Iterative correction of Hi-C data reveals hallmarks of chromosome organization. *Nat. Methods* **9**, 999–1003 (2012).
98. Marco-Sola, S., Sammeth, M., Guigó, R. & Ribeca, P. The GEM mapper: fast, accurate and versatile alignment by filtration. *Nat. Methods* **9**, 1185–1188 (2012).
99. Open2C. Cooltools: enabling high-resolution Hi-C analysis in Python. *bioRxiv*, 2022.2010.2031.514564 (2022).

Acknowledgements

We thank the core facilities at the Center for Genomics and Oncological Research (GENYO), including the cytometry and microscopy units for excellent technical assistance. We also thank the Centro Nacional de Análisis Genómico (CNAG) and the proteomics facility at the Center for Genomic Regulation (CRG) for support with ChIP-seq, mRNA-seq and proteomic experiments. We are grateful to Maria-Elena Torres-Padilla for providing useful scientific advice during the review process. Work in the Landeira lab is supported by the Carlos III Health Institute from European funds under the Recovery, Transformation, and Resilience Plan, file code IHRC22/00007, pursuant to Resolution of the Management of the Carlos III Health Institute, O.A., M.P. of December 22, 2022, granting ISCIII-HEALTH Seal of Excellence subsidies, and funded by the European Union - NextGenerationEU, the Spanish ministry of science and innovation (PID2019-108108-100, EUR2021-122005, PID2022-137060NB-I00), the Andalusian regional government (PIER-0211-2019, PY20_00681), and the University of Granada (A-BIO-6-UGR20) grants. The Marti-Renom lab acknowledges support from the Spanish Ministry of Science and Innovation (PID2020-115696RB-I00) as well as the Catalan Government through the AGAUR agency (SGR 01127). The work in Sara R. Heras' lab was supported by the Spanish Ministry of Science and Innovation (PID2020-115033RB-I00, RYC-2016-21395, CNS2023-145402) and the Andalusian regional government (PY20_00619 y A-CTS-28_UGR20) grants. We thank the IMPULSE visitor programme Severo Ochoa 2022 for funding Amador Gallardo to carry out chromosome conformation capture experiments at the CRG. Efres Belmonte Reche was supported by a Maria Zambrano fellowship financed by NextGenerationEU/European Union.

Author contributions

D.L. designed and conceptualized the study. A.G., M.M.-M., J.D.-R., L.L.-O., J.X. and P.T.-R. designed, performed, and analysed bench experiments. E.B.-R., G.P., I.F.-R., J.X., N.B. M.M.-M. and M.A.M.-R. performed bioinformatic analyses. S.R.-H., A.S.-P., A.M.-E., and M.A.M.-R. provided scientific advice and resources. A.G. and D.L. wrote the manuscript. All authors provided scientific feedback. D.L. obtained funding and supervised research.

Competing interests

The authors declare no competing interests.

Additional information

Supplementary information The online version contains supplementary material available at https://doi.org/10.1038/s41467-025-63778-4.

Correspondence and requests for materials should be addressed to David Landeira.

Peer review information *Nature Communications* thanks Miguel Branco, Haruhiko Siomi and the other anonymous reviewer(s) for their contribution to the peer review of this work. A peer review file is available.